

Article

Estimation of Electrical Conductivity and Magnetization Parameter of Neutron Star Crusts and Applied to the High-Braking-Index Pulsar PSR J1640-4631

Hui Wang ^{1,2,3}, Zhi-Fu Gao ^{1,2,*}, Huan-Yu Jia ³, Na Wang ¹ and Xiang-Dong Li ^{4,5}

¹ Xinjiang Astronomical Observatory, Chinese Academy of Sciences, 150, Science 1-Street, Urumqi 830011, China; gjwang@my.swjtu.edu.cn (H.W.); na.wang@xao.ac.cn (N.W.)

² Key Laboratory of Radio Astronomy, Chinese Academy of Sciences, West Beijing Road, Nanjing 210008, China

³ School of Physical Science and Technology, Southwest Jiao tong University, Chengdu 610031, China; hyjia@swjtu.cn

⁴ School of Astronomy and Space Science, Nanjing University, Nanjing 210023, China; lixd@nju.edu.cn

⁵ Key Laboratory of Modern Astronomy and Astrophysics (Nanjing University), Ministry of Education, Nanjing 210023, China

* Correspondence: zhifugao@xao.ac.cn

Received: 26 February 2020; Accepted: 22 April 2020; Published: 1 May 2020



Abstract: Young pulsars are thought to be highly magnetized neutron stars (NSs). The crustal magnetic field of a NS usually decays at different timescales in the forms of Hall drift and Ohmic dissipation. The magnetization parameter $\omega_B \tau$ is defined as the ratio of the Ohmic timescale τ_{Ohm} to the Hall drift timescale τ_{Hall} . During the first several million years, the inner temperature of the newly born neutron star cools from $T = 10^9$ K to $T = 1.0 \times 10^8$ K, and the crustal conductivity increases by three orders of magnitude. In this work, we adopt a unified equations of state for cold non-accreting neutron stars with the Hartree–Fock–Bogoliubov method, developed by Pearson et al. (2018), and choose two fiducial dipole magnetic fields of $B = 1.0 \times 10^{13}$ G and $B = 1.0 \times 10^{14}$ G, four different temperatures, T, and two different impurity concentration parameters, Q, and then calculate the conductivity of the inner crust of NSs and give a general expression of magnetization parameter for young pulsars: $\omega_B \tau \simeq (1 - 50)B_0 / (10^{13} \text{ G})$ by using numerical simulations. It was found when $B \leq 10^{15}$ G, due to the quantum effects, the conductivity increases slightly with the increase in the magnetic field, the enhanced magnetic field has a small effect on the matter in the low-density regions of the crust, and almost has no influence the matter in the high-density regions. Then, we apply the general expression of the magnetization parameter to the high braking-index pulsar PSR J1640-4631. By combining the observed arrival time parameters of PSR J1640-4631 with the magnetic induction equation, we estimated the initial rotation period P_0 , the initial dipole magnetic field B_0 , the Ohm dissipation timescale τ_{Ohm} and Hall drift timescale τ_{Hall} . We model the magnetic field evolution and the braking-index evolution of the pulsar and compare the results with its observations. It is expected that the results of this paper can be applied to more young pulsars.

Keywords: neutron stars; conductivity; magnetization parameters; ohmic dissipation; hall drift

1. Introduction

As one of the most densest stars in the Universe, neutron stars (NSs) are the most important research objects in the field of high-energy astrophysics. Studying NSs can help us understand the properties of matter at extreme circumstances, and a series of extreme physical processes may occur in

the interior of NSs with high density and strong pressure. It is generally recognized that pulsars are thought to be fast-spinning NSs radiating energy from their rotational energy losses. The magnetic field of pulsars is the basis of studying various radiation models and the probe into their internal structures [1], which has received wide attention from researchers. The surface dipole magnetic field is the strongest and has a wide distribution: from $B \sim 10^8$ – 10^9 gauss (G) for millisecond pulsar, through $B \sim 10^{12}$ – 10^{13} G for normal radio pulsars, to $B \sim 10^{14}$ – 10^{15} G for magnetars whose radiations are powered by magnetic fields [2–6]. The main method used to determine these magnetic fields is to measure the spin period P of each pulsar and its first derivative \dot{P} . Assuming that the pulsar's rotational energy loss is completely dominated by magnetic dipole radiation (MDR), the surface dipole poloidal magnetic field strength at the polar gaps of pulsars, B_p , is inferred as

$$P\dot{P} = \frac{2\pi^2 R^6 \sin^2 \alpha}{3Ic^3} B_p^2, \quad (1)$$

where I and R are the moment of inertia and radius of the star, respectively, c is the speed of light in vacuum, and α is the angle between the rotational axis and the dipole axis (the magnetic inclination angle).

The magnetic field evolution, cooling, and radiation mechanism of pulsars have been studied extensively and deeply in recent years. In order to simulate the cooling process of a NS, we started with a crust at initial temperature $T = 10^9$ K [7,8], a typical value after formation of the crust, at most within hours after birth, and we force the temperature of the isothermal crust to vary according to [9]: $T(t) = 10^9(1 + t_6)^{-1/6}$, t_6 is the NS age in 10^6 years (yrs). If only modified URCA processes are operating [10,11], this approximation is valid during the neutrino-cooling era. This simple approximation is sufficient for capturing the main effect: as the NS's crust cools (10^9 K to 10^8 K in 1 million years), crustal conductivity increases gradually, the Hall drift term is becoming more and more important via the increase in the electron relaxation time. When a significant part of the crustal magnetic field is dissipated and/or it has become much closer a force-free configuration, the field decay continues on a much longer Ohmic timescale [12,13]. In order to study magnetic field dissipation in NS crusts from magnetars to isolated NSs, Pons and Geppert (2007) [9] first performed the long-term simulations of the non-linear magnetic field evolution in realistic NS crusts with a stratified electron number density, n_e , and temperature dependent conductivity, σ . The results show that Ohmic dissipation influenced by Hall drift takes place in NS crusts on a timescale of $\tau_{Ohm} \sim 10^6$ yrs. When the initial magnetic field has magnetar strength, the fast Hall drift results in an initial rapid dissipation stage lasting about 10^4 yrs, where stable configurations can last for 10^6 yrs. The effect of Hall drift depends on the initial field strength and structure and how fast the NS cools. During the Hall drift stage, the toroidal field is strongly rearranged and dissipated, after this stage the long-term evolution seems to select, generally, a predominantly quadrupolar/octupolar structure concentrated in the inner crust and which tends to be stronger close to the poles. It is expected that such magnetic rearrangement and relatively rapid decay will produce the observed consequences such as those seen in magnetars, such as giant flares, and outer bursts [2,3].

Previous studies on the Ohmic dissipation mainly focused on the decay of the NS crust magnetic field, which includes calculations of the Ohmic decay eigenmodes in the crust [14], self-similar solutions near the stellar surface [15], Ohmic dissipation equation [16,17] and the dissipation rates of multipole magnetic field [18]. Geppert and Urpin (1994) first studied magnetic field evolution in accreting neutron stars [19]. There are two factors that can slow down the magnetic field decay: the gravitational redshift effect and the intrinsic curved geometry of the spatial section [20]. Due to the effects of general relativity, the timescale of magnetic field decay increases, but keeps in the same order of magnitude in flat spacetime [21–23]. Very recently, Pons and Viganò (2019) [24] reviewed the basic theory describing the magneto-thermal evolution models of NSs, focusing on numerical techniques, and providing a battery of benchmark tests to be used as a reference for present and future code developments. Wang et al. (2019) [25] deduced an eigenvalue equation of Ohmic decay for ordinary NSs under the framework of general relativity, and used the magnetic spot formation and thermoplastic flow

heating model to explain the soft X-ray luminosity of PSR J1640-4631 and its high surface temperature. By calculating the toroidal field decay rate and magnetic energy decay rate, Chen et al. (2019) [26] found that for most of high X-ray luminosity magnetars, the toroidal field Ohmic decay can provide the observed soft X-ray radiations, while for low X-ray luminosity transient magnetars, their soft X-ray radiations may come from rotating energy losses.

In this work, we concentrate on the effects of the cooling of young pulsars (from $T(t) = 10^9$ K to $T(t) = 1 \times 10^8$ K) on the crustal conductivity, and the evolutions of magnetic field and spin-down during the first few million years.

The reminder of this paper is organized as follows: In Section 2, by combining the equation of state and using a practical program, we calculate the conductivity of NS inner crust, and give the range of magnetization parameters; In Section 3, we build a theoretical model, and apply the general expression of magnetization parameter obtained to the high-braking-index pulsar PSR J1640-4631; A summary is given in Section 4.

2. Electrical Conductivity

2.1. Magnetic Induction Equation

In practice, since the distributions of electron number density and electrical conductivity are not constant, the NS crustal magnetic field is more complex and the nonlinear evolution of the Hall term must be considered. Firstly, the induction equation for the evolution of magnetic field in general relativity is given by [13].

$$\frac{\partial \mathbf{B}}{\partial t} = -\nabla \times \left[\frac{c}{4\pi n_e} \left[\nabla \times (e^\Phi \mathbf{B}) \right] \times \mathbf{B} + \frac{c^2}{4\pi \sigma} \nabla \times (e^\Phi \mathbf{B}) \right], \quad (2)$$

where Φ is gravitational potential, e^Φ is the relativistic redshift correction ($e^\Phi = Z = (1 - \frac{2GM}{c^2 R})^{1/2}$). M is the neutron star mass, e is the electron charge, \mathbf{B} is the magnetic field, which includes the poloidal component \mathbf{B}_{pol} and the toroidal component \mathbf{B}_{tor} , σ is the conductivity parallel to the magnetic field. The above equation includes two different effects of the Hall drift and Ohmic dissipation, which act on two distinct timescales. The Hall drift timescale mainly depends on the initial magnetic field B_0 , the electron number density n_e and the typical magnetic field length-scale λ .

$$\tau_{Hall} = \frac{4\pi n_e e \lambda^2}{c B_0} = \frac{6.4}{B_{14}} \left(\frac{n_e}{10^{36} \text{ cm}^{-3}} \right) \left(\frac{\lambda}{\text{km}} \right)^2 \times 10^5 \text{ yrs}, \quad (3)$$

where λ is approximated as the thickness of the inner crust, that is $\lambda \approx R_c \sim (500-800) \text{ m}$, B_{14} is the magnetic field in units of 10^{14} G , the Ohmic dissipation timescale is dependent on σ and λ [25,26],

$$\tau_{Ohm} = \frac{4\pi \sigma \lambda^2}{c^2} = 4.5 \left(\frac{\sigma}{10^{24} \text{ s}^{-1}} \right) \left(\frac{\lambda}{\text{km}} \right)^2 \times 10^6 \text{ yrs}. \quad (4)$$

Inserting some typical numbers of σ , λ and n_e , we get the Ohmic dissipation timescale $\tau_{Ohm} \sim 10^6$ yrs, and the Hall drift timescale $\tau_{Hall} \sim (10^4 \sim 10^5)$ yrs [27–29], the Hall timescale is usually 1–2 orders of magnitude lower than the Ohmic timescale. The Hall drift term of Equation (3) is a consequence of the Lorentz force acting on the electrons. The tensor components of the electric conductivity are derived in the relaxation time approximation [30]. From Equations (3) and (4), we get the magnetization parameter:

$$\omega_B \tau \equiv \frac{\tau_{Ohm}}{\tau_{Hall}} = \frac{\sigma B_0}{n_e e c}. \quad (5)$$

Then, the first term on the right-hand side of Equation (3) becomes $\frac{c^2}{4\pi} \nabla \times \omega_B \tau [(\nabla \times \mathbf{B}) \times \mathbf{b}]$, here $\mathbf{b} = \mathbf{B}/B$ is the unit vector in the direction of the magnetic field \mathbf{B} , and B the magnetic field

strength. It is obvious that the Hall term is proportional to the magnetization parameter $\omega_B \tau$. If the value of $\omega_B \tau$ significantly exceeds unity, the Hall drift dominates, which results in a very different field evolution from the pure Ohmic case, and the electric conductivity perpendicular to the magnetic field will be suppressed by a large magnetization parameter [29]. For a typical NS with $B_0 = 10^{14}$ G, the magnetic field decay is initially dominated by the Hall drift, followed by pure Ohmic decay after proceeding on a timescale on the order of 10^6 years.

Depending on the strength and structure of the initial magnetic field B_0 , the Hall drift phase lasts for a few 10^3 – 10^4 yrs, characterized by a strong exchange of magnetic field energy between the poloidal component and toroidal component of the field and by the redistribution of magnetic field energy between different timescales. To further study the relationship between the ratio of Ohmic timescale to Hall timescale and the magnetic field, the conductivity and magnetization parameter of NS crusts must be calculated.

2.2. Calculations of Conductivity and Magnetization Parameter

The conductivity of NS crusts determines the magnetization parameter and the magnetic field decay timescales, and the change in conductivity also greatly affects the processes of the magnetic field evolution and the NS cooling. The crustal conductivity is contributed by the electron-phonon scattering and electron-impurity scattering. By definition [31], the conductivity can be expressed as

$$\frac{1}{\sigma} = \frac{1}{\sigma_{hp}} + \frac{1}{\sigma_{imp}}, \quad (6)$$

where σ_{hp} and σ_{imp} are conductivities due to the electron-phonon scattering and the electron-impurity scattering, respectively. The magnitude of the conductivity depends strongly on temperature T and density ρ , the latter spans six or more orders of magnitude. The third parameter determining σ is the impurity concentration, which is defined as $\rho = 1/n \times \sum_i n_i (Z - Z_i)^2$, where n is the total ion density and n_i is the density of impurity of the i -th species with charge Z_i , and Z is the ionic charge in the pure lattice [15]. Since the lower-density regions of the outer crust have a significantly shorter Ohmic decay timescale and will not be included in our model.

On the basis of the previous work [32], Pearson et al. (2018) [33] used nuclear energy-density functional theory to develop a unified treatment of NSs within the framework of the picture of “cold catalysed matter”, meaning that thermal, nuclear and beta equilibrium prevail at a temperature T low enough that thermal effects can be neglected for the composition and pressure. By making use of the latest experimental nuclear mass data [34] and applying the Hartree–Fock–Bogoliubov (HFB) calculation method of nuclear interactions between two-body and three-body, they gave a set of nuclear mass models HFB-22, HFB-23, HFB-24, HFB-25 and HFB-26, corresponding to the energy-density functionals for BSk22, BSk23, BSk24, BSk25 and BSk26, respectively. In this way, each functional was used to calculate the composition, pressure density relationship and chemical potential of neutron stars, and study the influence of the uncertainty of symmetry energy on the calculation results. The fitting results of Pearson et al. (2018) support the heaviest neutron star that had been observed (the mass of the PSR J1614-2230 is $M = 2.01 \pm 0.04 M_\odot$ [35]). The EoS of homogeneous pure neutron matter (NeuM) provided by Li and Schulze (2008) [36] to which they fitted BSk22-25 can be regarded as typically hard, while the APR EoS provided by Akmal, Pandharipande and Ravenhall (1998) [37] to which they fitted BSk26 as typically soft. However, in the inner crust denser region of NSs, the fitting of EoS by BSk22 was uncertain, so it cannot be compared with other functionals. BSk24 and BSk26 have the same symmetric energy coefficient ($J = 30$ MeV) and the former has a larger value of symmetry-slope coefficient L . Since the symmetric energy coefficient ($J = 31$ MeV) of BSk23 is between BSk22 and BSk24, BSk23 is not considered in this paper. A detailed comparison of the above five functionals was given in Person et al. (2018). In Table 1 we list principle values of computed equilibrium proton number Z_{eq} in the inner crust below proton drip for functionals BSk22, BSk24, BSk25 and BSk26. The crustal baryon number density n_B always can be treated as an invariable quantity even in a strong magnetic

field, the electron fraction is equal to the proton number fraction Y_p , then the electron number density calculated as $n_e = Y_e \bar{n} = Z_{eq} \bar{n} / A$, where Z_{eq} is the computed equilibrium proton number, \bar{n} is the mean baryon number density, and A is the mass number of the nucleus.

Table 1. Principal values of Z_{eq} in the inner crust below proton drip for BSk22, BSk24, BSk25 and BSk26. Here \bar{n}_{min} and \bar{n}_{max} are the minimum and maximum baryon number densities, respectively, at which the nuclide is present.

EoS	Z_{eq}	$\bar{n}_{min} \text{ (fm}^{-3}\text{)}$	$\bar{n}_{max} \text{ (fm}^{-3}\text{)}$
BSk22	40	2.69×10^{-4}	0.0340
BSk24	40	2.56×10^{-4}	0.0715
BSk25	50	2.70×10^{-4}	0.0138
BSk26	40	2.61×10^{-4}	0.0730

In this article, implementing realistic conductivity profiles provided by Potekhin, Pons, and Page (2015) [38] (<http://www.ioffe.ru/astro/conduct>) into the code and combining with the EoS, we calculate the NS inner crustal conductivity. Since the effect of a strong magnetic field on the electrical conductivity was taking into account in reference [38], our results will be more reliable and will better reflect the actual situation of the NS crustal conductivity, compared with previous calculations.

Since the lattice phonons restrict the motion of electrons, the heat and charge transports are dominated by electron-phonon scattering at higher temperatures and lower densities, whereas heat and charge transport are dominated by the electron-impurity scattering at higher densities. In references [29,31], the authors studied the low-density crust dominated by electron-phonon scattering and gave a range of impurity parameter $Q \sim 10^{-4}$ – 10^{-2} , recently, studies of the high-density layers dominated by electron-impurity scattering suggested higher impurity parameters $Q \geq 1$ [25–27].

A newly born NS is very hot, its crustal temperature can be high as 10^9 K, and the neutrino radiation cooling dominates. Firstly, we choose a crust with a fiducial magnetic field $B = 1.0 \times 10^{13}$ G, and two different impurity parameters $Q = 0.01$ and $Q = 1.0$, when the temperature cools from 10^9 K to 5×10^8 K, then calculate partial values of the conductivity σ and magnetized parameter $\omega_B \tau$. Because of the suppression of the conductivity in the direction orthogonal to a strong magnetic field, here we only consider the conductivity parallel to the direction of the magnetic field. The unit of magnetization parameter $\omega_B \tau$ is in units of $B_0 / (10^{13} \text{ G})$, and the crust is thought to be isothermal. The calculated results are listed in Table 2.

It is found that (1) σ and $\omega_B \tau$ increase with the increase in ρ when T , Q and B_p are given; (2) σ and $\omega_B \tau$ decrease with the increase in Q when T , ρ and B_p are given; (3) σ and $\omega_B \tau$ decrease with the increase in T when Q , ρ and B_p are given. We compare the results in the case of $Q = 0.01$ with those of $Q = 1.0$, and find that both the differences between conductivities and the differences between magnetization parameters are very small, and the magnetization parameters are distributed in a range of $\omega_B \tau \sim (10^{-1} - 3) B_0 / (10^{13} \text{ G})$.

Keeping the fiducial magnetic field constant, when the crustal temperature drops to $T = 1.0 \times 10^8$ K, we assume $Q = 0.01$ and $Q = 1.0$, then obtain the magnetization parameter's ranges $\omega_B \tau \sim (0.5 - 3) B_0 / (10^{13} \text{ G})$ and $\omega_B \tau \sim (0.5 - 2) B_0 / (10^{13} \text{ G})$, respectively. Table 3 lists partial values of σ and $\omega_B \tau$. From Table 3, one can see that the conductivity increases over one order of magnitude when we keep constant Q and ρ and let T drops by one order of magnitude. Keeping the fiducial magnetic field constant, when the crustal temperature drops to $T = 1.0 \times 10^8$ K, we assume $Q = 0.01$ and $Q = 1.0$, and obtain the magnetization parameter's ranges $\omega_B \tau \sim (4.9 - 51) B_0 / (10^{13} \text{ G})$ and $\omega_B \tau \sim (4.6 - 10) B_0 / (10^{13} \text{ G})$, respectively. Table 3 lists partial values of σ and $\omega_B \tau$.

Table 2. Partial values of electrical conductivity and magnetization parameter for two different temperatures T and two different impurity parameters Q in the inner crust of NSs for the nuclear mass models HFB-22, HFB-24 and HFB-26. The unit of magnetization parameter $\omega_B \tau$ is the normalized magnetic field $B_0 / (10^{13} \text{ G})$ when the dipolar magnetic field strength $B_0 = 1.0 \times 10^{13} \text{ G}$. Here the crust is assumed to be isothermal.

		1.0e8 K						1.0e9 K					
		Q = 0.01			Q = 1			Q = 0.01			Q = 1		
\bar{n}_b (fm ⁻³)	ρ (g cm ⁻³)	Y_e	n_e (cm ⁻³)	σ (s ⁻¹)	$\omega_B \tau$								
HFB-22													
2.700e-04	4.513e11	2.955e-01	7.979e34	6.56e22	0.571	6.51e22	0.567	3.52e22	0.306	3.50e22	0.305		
5.253e-04	8.790e11	1.839e-01	9.658e34	7.66e22	0.551	7.60e22	0.546	4.05e22	0.291	4.03e22	0.290		
8.778e-04	1.470e12	1.294e-01	1.136e35	8.82e22	0.539	8.75e22	0.535	4.60e22	0.281	4.58e22	0.280		
1.194e-03	2.000e12	1.058e-01	1.263e35	9.72e22	0.534	9.63e22	0.529	5.02e22	0.276	5.00e22	0.275		
1.593e-03	2.670e12	8.832e-02	1.407e35	1.08e23	0.533	1.06e23	0.523	5.51e22	0.272	5.48e22	0.270		
2.707e-03	4.540e12	6.510e-02	1.762e35	1.34e23	0.528	1.33e23	0.524	6.73e22	0.265	6.69e22	0.264		
3.726e-03	6.250e12	5.526e-02	2.059e35	1.58e23	0.533	1.56e23	0.526	7.80e22	0.263	7.75e22	0.261		
4.994e-03	8.380e12	4.826e-02	2.410e35	1.88e23	0.542	1.85e23	0.533	9.11e22	0.262	9.05e22	0.260		
8.931e-03	1.500e13	3.841e-02	3.431e35	2.86e23	0.579	2.81e23	0.569	1.33e23	0.269	1.32e23	0.267		
1.535e-02	2.580e13	3.221e-02	4.944e35	4.75e23	0.667	4.63e23	0.650	2.11e23	0.296	2.08e23	0.292		
2.800e-02	4.713e13	2.691e-02	7.535e35	9.95e23	0.917	9.50e23	0.876	4.13e23	0.381	4.05e23	0.373		
3.400e-02	5.725e13	2.562e-02	8.709e35	1.36e24	1.084	1.28e24	1.021	5.51e23	0.439	5.38e23	0.429		
HFB-24													
2.570e-04	4.296e11	3.028e-01	7.783e34	6.44e22	0.575	6.39e22	0.570	3.46e22	0.309	3.44e22	0.307		
2.788e-04	4.660e11	2.859e-01	7.970e34	6.56e22	0.572	6.51e22	0.567	3.52e22	0.307	3.50e22	0.305		
5.253e-04	8.790e11	1.847e-01	9.703e34	7.70e22	0.551	7.63e22	0.546	4.06e22	0.291	4.05e22	0.290		
8.778e-04	1.470e12	1.325e-01	1.163e35	9.01e22	0.538	8.93e22	0.533	4.69e22	0.280	4.66e22	0.278		
1.194e-03	2.000e12	1.100e-01	1.314e35	1.01e23	0.534	9.97e22	0.527	5.18e22	0.274	5.15e22	0.272		
2.093e-03	3.510e12	8.114e-02	1.699e35	1.29e23	0.537	1.28e23	0.533	6.47e22	0.269	6.44e22	0.268		
2.707e-03	4.540e12	7.186e-02	1.945e35	1.48e23	0.528	1.46e23	0.521	7.33e22	0.262	7.29e22	0.260		
4.991e-03	8.380e12	5.661e-02	2.825e35	2.23e23	0.548	2.20e23	0.541	1.06e23	0.261	1.05e23	0.258		
8.926e-03	1.500e13	4.809e-02	4.293e35	3.77e23	0.610	3.69e23	0.597	1.71e23	0.277	1.69e23	0.273		
1.534e-02	2.580e13	4.289e-02	6.578e35	7.07e23	0.746	6.83e23	0.721	3.03e23	0.320	2.98e23	0.315		
2.778e-02	4.680e13	3.795e-02	1.054e36	1.66e24	1.094	1.55e24	1.021	6.64e23	0.437	6.46e23	0.426		
3.000e-02	5.055e13	3.729e-02	1.119e36	1.87e24	1.161	1.74e24	1.080	7.44e23	0.462	7.23e23	0.449		
5.000e-02	8.437e13	3.328e-02	1.664e36	4.93e24	2.057	4.27e24	1.782	1.83e24	0.764	1.73e24	0.722		
5.634e-02 *	9.510e13 *	3.279e-02	1.847e36	6.65e24	2.500	5.57e24	2.094	2.41e24	0.906	2.25e24	0.846		
HFB-26													
2.620e-04	4.379e11	2.996e-01	7.850e34	6.47e22	0.572	6.42e22	0.568	3.47e22	0.307	3.46e22	0.306		
2.788e-04	4.660e11	2.866e-01	7.988e34	6.56e22	0.570	6.51e22	0.566	3.52e22	0.306	3.50e22	0.304		
5.252e-04	8.790e11	1.833e-01	9.629e34	7.64e22	0.551	7.57e22	0.546	4.03e22	0.291	4.02e22	0.290		
8.777e-04	1.470e12	1.298e-01	1.139e35	8.83e22	0.538	8.75e22	0.533	4.60e22	0.280	4.58e22	0.279		
1.194e-03	2.000e12	1.066e-01	1.273e35	9.76e22	0.532	9.67e22	0.528	5.04e22	0.275	5.01e22	0.273		
1.593e-03	2.670e12	8.955e-02	1.427e35	1.09e23	0.530	1.07e23	0.521	5.54e22	0.270	5.51e22	0.268		
2.094e-03	3.510e12	7.668e-02	1.605e35	1.22e23	0.528	1.20e23	0.519	6.14e22	0.266	6.11e22	0.264		
2.707e-03	4.540e12	6.698e-02	1.813e35	1.37e23	0.525	1.36e23	0.521	6.86e22	0.263	6.82e22	0.261		
4.993e-03	8.380e12	5.098e-02	2.546e35	1.97e23	0.537	1.95e23	0.532	9.51e22	0.259	9.44e22	0.257		
8.929e-03	1.500e13	4.224e-02	3.772e35	3.16e23	0.582	3.10e23	0.571	1.45e23	0.267	1.44e23	0.265		
1.534e-02	2.580e13	3.758e-02	5.765e35	5.70e23	0.687	5.53e23	0.666	2.47e23	0.298	2.44e23	0.294		
2.778e-02	4.680e13	3.456e-02	9.601e35	1.36e24	0.984	1.28e24	0.926	5.41e23	0.391	5.29e23	0.383		
3.000e-02	5.054e13	3.425e-02	1.028e36	1.55e24	1.047	1.45e24	0.980	6.11e23	0.413	5.96e23	0.403		
5.000e-02	8.437e13	3.278e-02	1.639e36	4.44e24	1.881	3.89e24	1.648	1.62e24	0.686	1.54e24	0.652		
5.634e-02 *	9.510e13 *	3.274e-02	1.845e36	6.08e24	2.288	5.15e24	1.938	2.16e24	0.813	2.03e24	0.764		

* The sign denotes that the computed equilibrium proton number Z_{eq} begins to deviate from a standard value of $Z = 40$.

Table 3. Partial values of electrical conductivity and magnetization parameter for two different temperatures T and two different impurity parameters Q in the inner crust of NSs for the nuclear mass models HFB-22, HFB-24 and HFB-26. The unit of magnetization parameter $\omega_B\tau$ is the normalized magnetic field $B_0/(10^{13} \text{ G})$ when the dipolar magnetic field strength $B_0 = 1.0 \times 10^{13} \text{ G}$. Here the crust is assumed to be isothermal.

		1.0e7 K					1.0e8 K				
		Q = 0.01		Q = 1			Q = 0.01		Q = 1		
\bar{n}_b (fm ⁻³)	ρ (g cm ⁻³)	Y_e	n_e (cm ⁻³)	σ (s ⁻¹)	$\omega_B\tau$						
HFB-22											
2.700e-04	4.513e11	2.955e-01	7.979e34	4.77e25	415.15	7.38e24	64.23	5.64e23	4.91	5.30e23	4.61
5.253e-04	8.790e11	1.839e-01	9.658e34	6.19e25	445.08	8.12e24	58.39	7.00e23	5.03	6.51e23	4.68
8.778e-04	1.470e12	1.294e-01	1.136e35	7.65e25	467.65	8.77e24	53.61	8.51e23	5.20	7.84e23	4.79
1.194e-03	2.000e12	1.058e-01	1.263e35	8.81e25	484.41	9.21e24	50.64	9.71e23	5.34	8.87e23	4.88
1.593e-03	2.670e12	8.832e-02	1.407e35	1.02e26	503.44	9.68e24	47.78	1.11e24	5.48	1.01e24	4.98
2.094e-03	3.510e12	7.511e-02	1.573e35	1.18e26	520.94	1.02e25	45.03	1.28e24	5.65	1.15e24	5.08
3.726e-03	6.250e12	5.526e-02	2.059e35	1.72e26	580.11	1.15e25	38.79	1.83e24	6.17	1.59e24	5.36
4.994e-03	8.380e12	4.826e-02	2.410e35	2.16e26	622.41	1.23e25	35.44	2.28e24	6.57	1.94e24	5.59
8.931e-03	1.500e13	3.841e-02	3.431e35	3.74e26	756.99	1.44e25	29.15	3.89e24	7.87	3.09e24	6.25
1.535e-02	2.580e13	3.221e-02	4.944e35	7.06e26	991.66	1.70e25	23.87	7.24e24	10.17	5.11e24	7.18
2.781e-02	4.680e13	2.696e-02	7.498e35	1.66e27	1537.4	2.08e25	19.26	1.69e25	15.65	9.36e24	8.67
3.400e-02	5.725e13	2.562e-02	8.709e35	2.39e27	1905.8	2.25e25	17.94	2.43e25	19.38	1.17e25	9.33
HFB-24											
2.570e-04	4.296e11	3.028e-01	7.783e34	4.68e25	417.58	7.31e24	65.22	5.53e23	4.93	5.20e23	4.64
2.788e-04	4.660e11	2.859e-01	7.970e34	4.81e25	419.11	7.39e24	64.39	5.67e23	4.94	5.33e23	4.64
5.253e-04	8.790e11	1.847e-01	9.703e34	6.28e25	449.46	8.14e24	58.26	7.08e23	5.07	6.58e23	4.71
8.778e-04	1.470e12	1.325e-01	1.163e35	7.97e25	475.90	8.87e24	52.96	8.82e23	5.27	8.10e23	4.84
1.194e-03	2.000e12	1.100e-01	1.314e35	9.37e25	495.20	9.39e24	49.63	1.03e24	5.44	9.35e23	4.94
2.093e-03	3.510e12	8.114e-02	1.699e35	1.33e26	543.62	1.05e25	42.92	1.43e24	5.84	1.27e24	5.19
2.707e-03	4.540e12	7.186e-02	1.945e35	1.60e26	571.27	1.12e25	39.99	1.71e24	6.11	1.50e24	5.36
3.724e-03	6.250e12	6.288e-02	2.342e35	2.09e26	619.72	1.22e25	36.18	2.20e24	6.52	1.88e24	5.57
4.991e-03	8.380e12	5.661e-02	2.825e35	2.76e26	678.47	1.32e25	32.45	2.88e24	7.08	2.39e24	5.88
8.926e-03	1.500e13	4.809e-02	4.293e35	5.33e26	862.19	1.59e25	25.72	5.49e24	8.88	4.11e24	6.65
1.534e-02	2.580e13	4.289e-02	6.578e35	1.13e27	1192.9	1.92e25	20.27	1.15e25	12.14	7.25e24	7.65
2.778e-02	4.680e13	3.795e-02	1.054e36	2.96e27	1950.2	2.42e25	15.94	3.00e25	19.77	1.35e25	8.89
3.000e-02	5.055e13	3.729e-02	1.119e36	3.38e27	2097.6	2.50e25	15.51	3.44e25	21.35	1.45e25	9.00
5.000e-02	8.437e13	3.328e-02	1.664e36	9.59e27	4002.2	3.19e25	13.31	9.85e25	41.11	2.41e25	10.10
5.634e-02 *	9.510e13 *	3.279e-02	1.847e36	1.32e28	4963.0	3.43e25	12.90	1.36e26	51.13	2.74e25	10.30
HFB-26											
2.620e-04	4.379e11	2.996e-01	7.850e34	4.70e25	415.78	7.33e24	64.84	5.55e23	4.91	5.22e23	4.62
2.788e-04	4.660e11	2.866e-01	7.988e34	4.80e25	417.29	7.39e24	64.25	5.66e23	4.92	5.32e23	4.62
5.252e-04	8.790e11	1.833e-01	9.629e34	6.22e25	448.59	8.11e24	58.49	7.01e23	5.06	6.52e23	4.70
8.777e-04	1.470e12	1.298e-01	1.139e35	7.74e25	471.91	8.78e24	53.53	8.59e23	5.24	7.90e23	4.82
1.194e-03	2.000e12	1.066e-01	1.273e35	8.97e25	489.33	9.25e24	50.46	9.85e23	5.37	8.99e23	4.90
1.593e-03	2.670e12	8.955e-02	1.427e35	1.05e26	510.98	9.74e24	47.40	1.14e24	5.55	1.03e24	5.01
2.707e-03	4.540e12	6.698e-02	1.813e35	1.45e26	555.40	1.09e25	41.75	1.55e24	5.94	1.37e24	5.25
3.726e-03	6.250e12	5.756e-02	2.144e35	1.84e26	595.98	1.17e25	37.90	1.95e24	6.32	1.68e24	5.44
4.993e-03	8.380e12	5.098e-02	2.546e35	2.36e26	643.71	1.26e25	34.37	2.48e24	6.76	2.09e24	5.70
8.929e-03	1.500e13	4.224e-02	3.772e35	4.33e26	797.18	1.50e25	27.62	4.47e24	8.23	3.47e24	6.39
1.534e-02	2.580e13	3.758e-02	5.765e35	8.95e26	1078.1	1.80e25	21.68	9.13e24	11.00	6.10e24	7.35
2.778e-02	4.680e13	3.456e-02	9.601e35	2.44e27	1764.9	2.29e25	16.56	2.48e25	17.94	1.20e25	8.68
3.000e-02	5.054e13	3.425e-02	1.028e36	2.83e27	1911.7	2.37e25	16.01	2.87e25	19.39	1.31e25	8.85
5.000e-02	8.437e13	3.278e-02	1.639e36	8.88e27	3762.4	3.09e25	13.09	9.10e25	38.56	2.31e25	9.79
5.634e-02 *	9.510e13 *	3.274e-02	1.845e36	1.23e28	4629.6	3.34e25	12.57	1.27e26	47.80	2.65e25	9.97

* The sign denotes that the computed equilibrium proton number Z_{eq} begins to deviate from a standard value of $Z = 40$.

From Table 3, one can see that the conductivity increases over 1–2 order of magnitude when we keep constant Q and ρ and let T drops by one order of magnitude. Table 4 lists partial values of σ and $\omega_B\tau$ for the nuclear mass model HFB-25, we compare the results in the case of $Q = 0.01$ with those of $Q = 1.0$, and find that both the differences between conductivities and the differences between magnetization parameters are very small, and the magnetization parameters are distributed in a range of $\omega_B\tau \sim (4.0\text{--}10.0)B_0/(10^{13} \text{ G})$ and $\omega_B\tau \sim (4.0\text{--}7.0)B_0/(10^{13} \text{ G})$. If $\rho > 9.510 \times 10^{13} \text{ g cm}^{-3}$, the calculated equilibrium number of protons, as shown in the third column of Table 5, will deviate from a standard value of $Z = 40$. Finally, we assume a fiducial magnetic field $B_0 = 1.0 \times 10^{14} \text{ G}$,

and repeat the above calculations, and list partial results in Tables A1 and A2 in Appendix A. It is found that when $B \leq 10^{15}$ G, due to the quantum effects, the conductivity increases slightly with the increase in the magnetic field, the enhanced magnetic field has a small effect on the matter in the low-density regions of the crust, and almost has no influence the matter in the high-density regions. Note that, this weak dependence of the longitudinal conductivity on the magnetic field is not absolute, it applies only to relatively large densities and not too strong magnetic fields. If the field strength is far larger than 10^{15} G, there will be significant quantum effects of conductivity, such as oscillations around the classical value.

Table 4. Same as in Table 3, for the nuclear mass model HFB-25 (Cited from Person et al. (2008)).

\bar{n}_b (fm ⁻³)	ρ (g cm ⁻³)	Z_{eq}	n_e (cm ⁻³)	1.0e7 K				1.0e8 K			
				Q = 0.01		Q = 1		Q = 0.01		Q = 1	
				σ (s ⁻¹)	$\omega_B \tau$						
2.800e-04	4.681e11	49.99	7.970e34	4.24e25	369.4	8.68e24	75.63	5.05e23	4.40	4.82e23	4.20
5.000e-04	8.366e11	49.99	9.629e34	5.47e25	394.5	9.62e24	69.38	6.26e23	4.51	5.94e23	4.28
1.000e-03	1.675e12	49.99	1.258e35	7.82e25	431.7	1.10e25	60.72	8.70e23	4.80	8.15e23	4.50
5.000e-03	8.397e12	49.99	3.162e35	3.04e26	667.7	1.71e25	37.56	3.19e24	7.01	2.71e24	5.95
1.000e-02	1.682e13	49.99	5.464e35	7.70e26	978.6	2.19e25	27.83	7.92e24	10.07	5.86e24	7.45

Table 5. Comparison of the nuclear mass models HFB-24 and HFB-26 in the higher matter-density layers. The third column denotes the computed equilibrium proton number, and the other parameters are the same as in Table 3.

\bar{n}_b (fm ⁻³)	ρ (g cm ⁻³)	Z_{eq}	n_e (cm ⁻³)	1.0e7 K				1.0e8 K			
				Q = 0.01		Q = 1		Q = 0.01		Q = 1	
				σ (s ⁻¹)	$\omega_B \tau$						
HFB-24											
5.000e-02	8.437e13	39.91	1.664e36	9.59e27	4002.2	3.19e25	13.31	9.85e25	41.11	2.41e25	10.10
5.634e-02	9.510e13	39.80	1.847e36	1.32e28	4963.0	3.43e25	12.90	1.36e26	51.13	2.74e25	10.30
5.923e-02	1.000e14	39.65	1.936e36	1.53e28	5488.1	3.55e25	12.73	1.59e26	57.03	2.91e25	10.44
7.000e-02	1.182e14	53.54	2.297e36	3.07e28	9281.4	5.73e25	17.32	3.24e26	97.95	4.88e25	14.75
7.150e-02	1.208e14	55.26	2.350e36	3.42e28	10106.4	6.14e25	18.14	3.62e26	107.0	5.26e25	15.54
HFB-26											
5.000e-02	8.437e13	39.91	1.639e36	8.88e27	3762.4	3.09e25	13.09	9.10e25	38.56	2.31e25	9.79
5.634e-02	9.510e13	39.82	1.845e36	1.23e28	4629.6	3.34e25	12.57	1.27e26	47.80	2.65e25	9.97
6.513e-02	1.100e14	39.31	2.156e36	1.96e28	6313.1	3.73e25	12.01	2.05e26	66.03	3.16e25	10.18
7.000e-02	1.183e14	38.47	2.348e36	2.56e28	7571.5	3.97e25	11.74	2.71e26	80.15	3.47e25	10.26
7.300e-02	1.233e14	37.33	2.475e36	3.02e28	8473.6	4.13e25	11.59	3.23e26	90.63	3.67e25	10.30

To vividly describe the changes of conductivity and magnetization parameter with different values of T , ρ and B , we make diagrams of $\sigma, \omega_B \tau$ versus ρ , according to the above calculations. As shown in Figure 1, the NS crustal conductivity varies by 3–4 orders of magnitude. A high impurity content could lead to even faster dissipation. Since $B_{13} = B_0/(10^{13} \text{ G})$ and $B_{14} = B_0/(10^{14} \text{ G})$, by comparing Figure 1a with Figure 1b, Figure 1c with Figure 1d, Figure 1e with Figure 1f, and Figure 1g with Figure 1h, we do not find significant differences in the simulations with $B = 1 \times 10^{13} \text{ G}$ and $B = 1 \times 10^{14} \text{ G}$. According to the above results, for a strongly magnetized NS, when the crustal temperature drops from 10^9 K to $1.0 \times 10^8 \text{ K}$, the ratio of the Ohmic dissipation timescale to the Hall drift timescale is approximately

$$\omega_B \tau = \frac{\tau_{Ohm}}{\tau_{Hall}} = (1 - 50) \times \frac{B_0}{10^{13} \text{ G}}. \tag{7}$$

According to Equation (7), the magnetization parameter increases linearly with the initial magnetic field strength B_0 . To ensure that the Ohmic dissipation timescale is not less than the Hall

drift timescale, and to ensure that our fit is consistent with most models of the magnetic field evolution of NSs, we omit the value of $\omega_B \tau \sim 10^{-1}$.

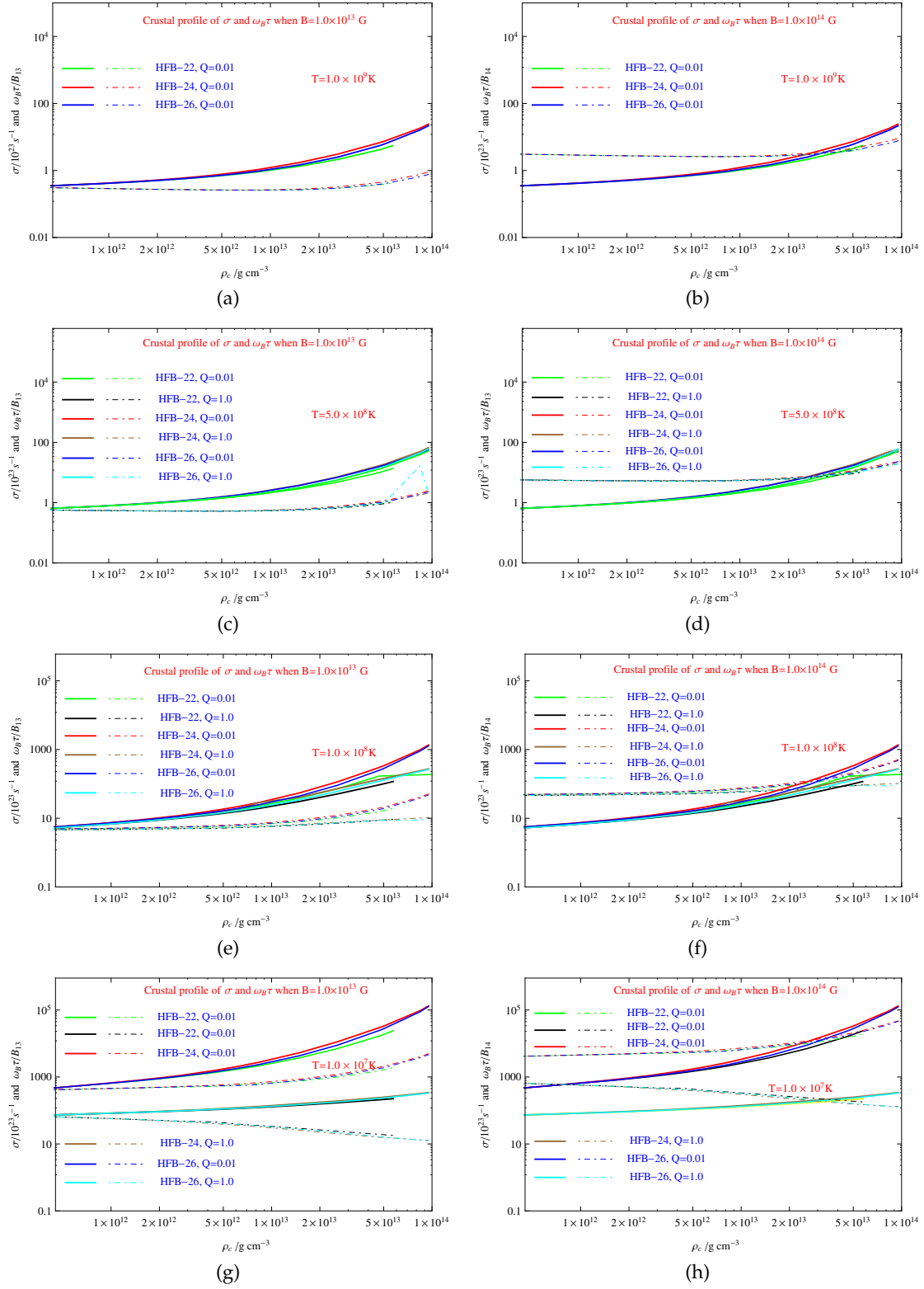


Figure 1. The relations of σ , $\omega_B \tau$ and ρ in the inner crust of a neutron star. The solid line and dot-dashed line are for σ and $\omega_B \tau$, respectively. In (a,c,e,g), the fiducial magnetic field is $B = 1.0 \times 10^{13}$ G; In (b,d,f,h), the fiducial magnetic field is $B = 1.0 \times 10^{14}$ G. The crust is assumed to be isothermal.

It is worth noting that such averaged timescales in Equation (7) are of very restricted use in characterizing the field evolution in NS crusts, since the density vary over many orders of magnitude there. A different issue is whether or not this effect is observable when studying populations of older NSs. Since the conductivity strongly depends on temperature, the Ohmic dissipation timescale increases significantly as the NS crustal temperature cools to $T \leq 10^7$ K (usually 10^7 years after birth corresponding to $\omega_B \tau \sim 10^{7-8}$ yrs.), and there is no rapid field decay after that age. So in this paper, we want to focus on the evolution of magnetic fields in relatively young pulsars.

3. Applying the Magnetization Parameter Expression to the High-Braking-Index Pulsar PSR J1640-4631

3.1. The Braking Index and Radiation Characteristics of PSR J1640-4631

Due to the existence of energy loss mechanisms, such as electromagnetic radiation, particle stellar wind, strong neutrino flow and gravitational radiation [39,40], a pulsar spins down. An important and measurable quantity closely related to a pulsar’s rotational evolution is the braking index n , defined by assuming that the star spins down in the light of a power law

$$\dot{\Omega} = -K\Omega^n, \tag{8}$$

where Ω is the angular velocity, $\dot{\Omega}$ is the first time derivative of Ω , and K is a proportionality constant. According to the standard method, the braking index is defined as

$$n = \frac{\Omega \ddot{\Omega}}{\dot{\Omega}^2} = \frac{v \ddot{v}}{\dot{v}^2} = 2 - \frac{P \ddot{P}}{\dot{P}^2}, \tag{9}$$

where $\ddot{\Omega}$ is the second time derivative of Ω , $v = \Omega/2\pi$ is the spin frequency, \dot{P} and \ddot{P} are the first time derivative and the second time derivative of P , respectively. When the magneto-dipole radiation (MDR) solely causes the pulsar to spin down, the braking index is predicted to be $n = 3$. Up to date, only 9 of the ~ 3000 known pulsars have reliably measured braking indices, all of which deviate from 3, demonstrating that the spin-down mechanism is not pure MDR. In the case of a varying dipole magnetic field at the pole B_p , the braking index n can be simply expressed as follows [13].

$$n = 3 - 4\tau_c \frac{\dot{B}_p}{B_p}, \tag{10}$$

where $\tau_c = P/2\dot{P}$ is the characteristic age, \dot{B}_p is the time derivative of B_p . For an increasing B_p , we will always obtain $n < 3$, owing to an increasing dipole braking torque, whereas $n > 3$ for a decreasing B_p .

Recently, PSR J1640-4631, associated with the TeV γ -ray source HESS J1640-465 was discovered using the *NuSTAR* X-ray observatory [41]. Based on its timing observational data $P = 206.4$ ms, $\dot{P} = 9.7228 \times 10^{-13}$ s s⁻¹, and $\ddot{P} = -5.27(13) \times 10^{-24}$ s s⁻², Archibald et al. [42] derived its braking index to be $n = 3.15(3)$ (here and following all digits in parentheses denote the standard uncertainty), corresponding to its characteristic age $\tau_c = 3550$ yrs. A pulsar’s true age t_{age} can be estimated by the age of its associated supernova remnant(SNR), t_{SNR} , because it is universally considered that pulsars originate from supernova explosions. G338.3-0.0 is a shell-type SNR and spatially relates to HESS J1640-465, which is considered to be the most luminous γ -ray source in the Galaxy. The X-ray pulsar PSR J1640-4631 was recently discovered within the shell of SNR G338.3-0.0. Unfortunately, no X-ray emission was detected from the shell of the SNR, thus, the true age of PSR J1640-4631 cannot be estimated from Equation (4) in Reference [12]. The pulsar’s true age can be estimated by the following expression [13]

$$t = \frac{P}{(n-1)\dot{P}} \left[1 - \left(\frac{P_0}{P} \right)^{n-1} \right], \quad (n \neq 1)$$

$$t = 2\tau_c \ln\left(\frac{P}{P_0}\right), \quad (n = 1). \quad (11)$$

Inserting the values of P and \dot{P} into Equation (11), we estimate the true age of PSR J1640-4631 to be $t_{age} \approx 3130$ yrs. The soft X-ray radiation flux F_X [2–10 keV] of PSR J1640-4631 obtained from *Chandra* + *NuStar* telescopes is given by $F_X = 1.8(4) \times 10^{-13}$ erg cm⁻² s⁻¹ [41]. Assuming that the observed X-ray radiation from PSR J1640-4631 is isotropic, the soft X-ray luminosity is estimated as $L_X = 4\pi d^2 F_X = 3.26(72) \times 10^{33}$ erg s⁻¹, where $d = 12$ kpc is the distance from G338.3-0.1 to Earth [43]. According to the blackbody thermal radiation, the surface temperature of the star is estimated as $T_s = (L_X/4\pi R^2 \sigma_{SB})^{1/4} \approx 1.54(6) \times 10^6$ K, where σ_{SB} is the Stefan-Boltzmann constant. This value of T is much higher than $T_s \sim 10^5$ K for common radio pulsars, but it is very near to the observed surface temperatures of magnetars. Recently, Wang et al. (2019) [25] found that observed X-ray flux of the pulsar could be caused by the decay of a multipolar magnetic field near the pole, which is strong enough to activate the slot-gap mechanism. The high surface temperature of the star is attributed either to magnetic spot formation [4] or thermoplastic wave heating due to the decay of the toroidal field near the pole [43].

3.2. Theoretical Model of Dipole Magnetic Field Evolution

The maximum NS mass predicted by EoS is model dependent. The largest sample of measured NS masses available for analysis is publicly accessible online at <http://www.stellarcollapse.org/>, from which one can get a range of about (1–2) M_\odot for the observational NS masses. To date, the relativistic-mean-field (RMF) theory has become a standard method to study nuclear matter and finite-nuclei properties [44–48], but it has not been possible to fit masses in the RMF framework with a precision at all comparable to what was achieved with Skyrme functionals (Pearson et al. (2018) [33]). At high densities the symmetry energy of BSk26 increases much less steeply than that of BSk24, given the much softer EoS of NeuM to which it was fitted (Pearson et al. 2018). In this paper, we choose a medium-mass NS with $M = 1.45M_\odot$ and $R = 11.5$ km, corresponding to the moment of inertia $I = 1.34(1) \times 10^{45}$ g cm² for PSR J1640-4631 in the BSK26 EoS.

The evolution of the crustal magnetic field is phenomenologically divided into evolutionary stages: the initial stage with rapid (non-exponential) decay, and a later stage with purely Ohmic dissipation (exponential). For simplicity and for qualitatively investigating the effects of the magnetic field decay, the geometry of the field is assumed to be fixed, and the temporal dependence is included only in the normalized B_p according to

$$B_p(t) = B_0 \frac{\exp(-Zt/\tau_{Ohm})}{1 + \frac{\tau_{Ohm}}{\tau_{Hall}} [1 - \exp(-Zt/\tau_{Ohm})]}, \quad (12)$$

where the effect of general relativity is considered, and the gravitational redshift factor $Z = (1 - \frac{2GM}{c^2 R})^{1/2} \approx 0.9$. The inclusion of Hall drift accelerates the decay of the magnetic field, especially in the early field evolution when $t \ll t_{Ohm}$, during which the Hall term becomes a dominant factor, as given by $B_p \approx B_0(1 + t/\tau_{Hall})^{-1}$. Taking the first derivative of the dipole field with respect to time, we obtain

$$\frac{dB_p}{dt} = \frac{-ZB_p}{\tau_{Ohm}} - \frac{ZB_p^2}{\tau_{Hall}B_0}. \quad (13)$$

If the magnetic field evolution of PSR J1640-4631 cannot be ignored and the dipole braking still dominates, according to Reference [43], the braking law of the pulsar is reformulated as

$$\dot{v}(t) = \frac{2\pi^2 R^6}{3Ic^3} B_p^2(t) v^3(t), \tag{14}$$

where $B_p(t)$ is determined by Equation (12), and a constant inclination angle $\alpha = 90^\circ$ is assumed for the sake of simplicity. Integrating Equation (14) gives the pulsar's spin frequency

$$v^{-2} = v_0^{-2} + 2 \int_0^t \frac{2\pi^2 R^6}{3Ic^3} B_p^2(t') dt'. \tag{15}$$

From Equation (15), we obtain the relation between the rotational period and time

$$P(t) = [P_0^2 + 2 \int_0^t \frac{2\pi^2 R^6 B_0^2}{3Ic^3} \frac{\exp^2(-Zt'/\tau_{Ohm})}{[1 + \frac{\tau_{Ohm}}{\tau_{Hall}} [1 - \exp(-Zt'/\tau_{Ohm})]]^2} dt']^{1/2}. \tag{16}$$

Let $x = -Zt/\tau_{Ohm}$, then $dt = -\frac{\tau_{Ohm}}{Z} dx$ the second term in Equation (16) becomes

$$\begin{aligned} \text{Second} &= 2 \int_0^t \frac{2\pi^2 R^6 B_0^2}{3Ic^3} \frac{\exp^2(-Zt'/\tau_{Ohm})}{[1 + \omega_B \tau [1 - \exp(-Zt'/\tau_{Ohm})]]^2} dt' \\ &= \frac{4\pi^2 R^6 B_0^2}{3Ic^3} \cdot \frac{-\tau_{Ohm}}{Z(\omega_B \tau)^2} \cdot \int_0^x \frac{e^{2x}}{[1 + \frac{1}{\omega_B \tau} - e^x]^2} dx. \end{aligned} \tag{17}$$

Making the following substitutions: $a = 1 + \frac{1}{\omega_B \tau}$ and $k = a - e^x$, then we have $x = \ln(a - k)$ and $dx = -\frac{1}{a-k} dk$. Inserting the above substitutions into Equation (17), we get

$$\begin{aligned} \text{Second} &= \frac{4\pi^2 R^6 B_0^2}{3Ic^3} \cdot \left(\frac{-\tau_{Ohm}}{Z(\omega_B \tau)^2} \right) \cdot \int_{a-1}^{a-\exp(x)} \left(\frac{a-k}{k} \right)^2 \frac{-1}{a-k} dk \\ &= \frac{4\pi^2 R^6 B_0^2}{3Ic^3} \cdot \left(\frac{\tau_{Ohm}}{Z(\omega_B \tau)^2} \right) \cdot \int_{a-1}^{a-\exp(x)} \left(\frac{a}{k^2} - \frac{1}{k} \right) dk \\ &= \frac{4\pi^2 R^6 B_0^2}{3Ic^3} \cdot \left(\frac{\tau_{Ohm}}{Z(\omega_B \tau)^2} \right) \cdot \left[a \left[-\frac{1}{k} \right]_{a-1}^{a-\exp(x)} - [\ln(k)]_{a-1}^{a-\exp(x)} \right] \\ &= \frac{4\pi^2 R^6 B_0^2 \tau_{Ohm}}{3Ic^3 Z (\omega_B \tau)^2} \left[\frac{a}{a-1} - \frac{a}{a-e^x} + \ln(a-1) - \ln(a-e^x) \right], \end{aligned} \tag{18}$$

where $k = a - 1$ if $x = 0$. Then Equation (16) is rewritten as

$$P(t) = \left[P_0^2 + \frac{4\pi^2 R^6 B_0^2 \tau_{Ohm}}{3Ic^3 Z (\omega_B \tau)^2} \left[\frac{a}{a-1} - \frac{a}{a-e^x} + \ln(a-1) - \ln(a-e^x) \right] \right]^{1/2}. \tag{19}$$

For convenience, the period $P(t)$ is denoted as $P(t) = N^{1/2}(t)$,

$$N(t) = \left[P_0^2 + \frac{4\pi^2 R^6 B_0^2 \tau_{Ohm}}{3Ic^3 Z (\omega_B \tau)^2} \left(\frac{a}{a-1} - \frac{a}{a-e^x} + \ln(a-1) - \ln(a-e^x) \right) \right]. \tag{20}$$

Taking the derivative of $P(t)$ with respect to time, we get the time first derivative of the period,

$$\dot{P}(t) = \frac{1}{2} N^{-1/2} \frac{4\pi^2 R^6 B_0^2 \tau_{Ohm}}{3Ic^3 (\omega_B \tau)^2 Z} \left[\ln(a-1) + \frac{a}{a-1} - \frac{a}{a-e^x} - \ln(a-e^x) \right]'. \tag{21}$$

Taking the derivatives of all the terms in parentheses of Equation (21) with respect to time t , we have

$$[\dots]' = \frac{z}{\tau_{Ohm}} \frac{e^{-Zt/\tau_{Ohm}}}{a - e^{-Zt/\tau_{Ohm}}} \left(\frac{a}{a - e^{-Zt/\tau_{Ohm}}} - 1 \right) = \frac{Z}{\tau_{Ohm}} \frac{e^{-2Zt/\tau_{Ohm}}}{(a - e^{-Zt/\tau_{Ohm}})^2}. \tag{22}$$

Equation (21) then becomes

$$\dot{P}(t) = \frac{2\pi^2 R^6 B_0^2}{3Ic^3 (\omega_B \tau)^2} \frac{e^{-2Zt/\tau_{Ohm}}}{(a - e^{-Zt/\tau_{Ohm}})^2} N^{-1/2} = \frac{2\pi^2 R^6 B_0^2}{3Ic^3 (\omega_B \tau)^2} \frac{e^{-2Zt/\tau_{Ohm}}}{(a - e^{-Zt/\tau_{Ohm}})^2} P(t)^{-1}. \tag{23}$$

Similarly, taking the derivative of $\dot{P}(t)$ with respect to time, the second derivative of the period can be expressed as

$$\begin{aligned} \ddot{P}(t) &= - \left(\frac{2\pi^2 R^6 B_0^2}{3Ic^3 (\omega_B \tau)^2} \right)^2 \frac{e^{-4Zt/\tau_{Ohm}} N^{-3/2}}{(a - e^{-Zt/\tau_{Ohm}})^4} - \frac{4\pi^2 R^6 B_0^2 Z}{3Ic^3 (\omega_B \tau)^2 \tau_{Ohm}} \frac{ae^{-2Zt/\tau_{Ohm}} N^{-1/2}}{(a - e^{-Zt/\tau_{Ohm}})^3} \\ &= - \left[\frac{2\pi^2 R^6 B_0^2}{3Ic^3 (\omega_B \tau)^2} \right]^2 \frac{e^{-4Zt/\tau_{Ohm}}}{(a - e^{-Zt/\tau_{Ohm}})^4} P(t)^3 - \frac{4\pi^2 R^6 B_0^2 Z}{3Ic^3 (\omega_B \tau)^2 \tau_{Ohm}} \frac{ae^{-2Zt/\tau_{Ohm}}}{(a - e^{-Zt/\tau_{Ohm}})^3} P(t). \end{aligned} \tag{24}$$

From the expression of $\dot{P}(t)$, we obtain

$$\frac{2\pi^2 R^6 B_0^2}{3Ic^3 (\omega_B \tau)^2} = \dot{P}(t) P(t) (a - e^{-Zt/\tau_{Ohm}})^2 e^{2Zt/\tau_{Ohm}}. \tag{25}$$

Plugging the expression of $\ddot{P}(t)$ into Equation (25), we further simplify Equation (25) as

$$\begin{aligned} \ddot{P}(t) &= - \left[\dot{P}(t) P(t) (a - e^{-Zt/\tau_{Ohm}})^2 e^{2Zt/\tau_{Ohm}} \right]^2 \times \frac{e^{-4Zt/\tau_{Ohm}}}{(a - e^{-2Zt/\tau_{Ohm}})^4 P(t)^3} \\ &\quad - \frac{2Z\dot{P}(t)P(t) (a - e^{-Zt/\tau_{Ohm}})^2 e^{2Zt/\tau_{Ohm}}}{\tau_{Ohm}} \cdot \frac{ae^{-2Zt/\tau_{Ohm}}}{(a - e^{-Zt/\tau_{Ohm}})^3 P(t)} \\ &= -\dot{P}^2(t)P(t)^{-1} - \frac{2Za\dot{P}(t)}{\tau_{Ohm} (a - e^{-Zt/\tau_{Ohm}})}. \end{aligned} \tag{26}$$

Rearranging Equation (26), we obtain a very useful expression

$$\frac{\ddot{P}(t)}{\dot{P}(t)} + \frac{\dot{P}(t)}{P(t)} = \frac{-2Z \left(1 + \frac{1}{\omega_B \tau} \right)}{\left(1 + \frac{1}{\omega_B \tau} - \exp(-Zt/\tau_{Ohm}) \right) \tau_{Ohm}}. \tag{27}$$

Inserting Equation (9) into Equation (27), we obtain

$$(n - 3) \frac{\dot{P}(t)}{P} = \frac{-2Z \left(1 + \frac{1}{\omega_B \tau} \right)}{\left(1 + \frac{1}{\omega_B \tau} - \exp(-Zt/\tau_{Ohm}) \right) \tau_{Ohm}}. \tag{28}$$

Inserting $P = 206.4$ ms, $\dot{P} = 9.7728 \times 10^{-13}$ s s⁻¹ and $\ddot{P} = -5.27(13) \times 10^{-24}$ s s⁻² into Equation (27), the left side of Equation (27) is equal to -7.09×10^{-13} s⁻¹. Substituting the gravitational redshift $Z = 0.9$ into Equation (27), then we make a plot of Ohmic dissipation timescale τ_{Ohm} versus magnetization parameter $\omega_B \tau$ by method of numerical simulations, as shown in Figure 2.

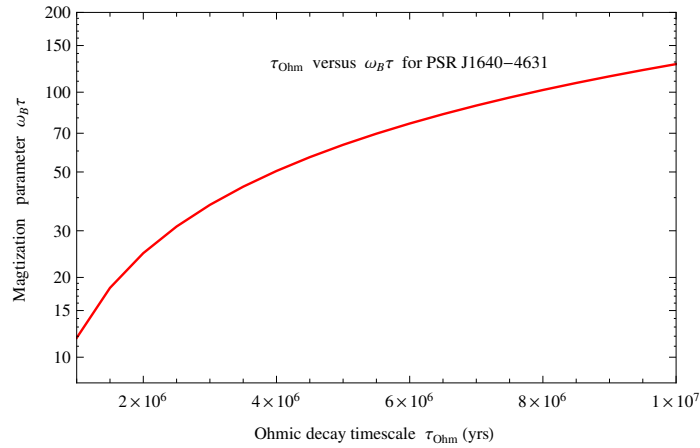


Figure 2. The relation of τ_{Ohm} and $\omega_B\tau$ for PSR J1640-4631.

Figure 2 clearly shows that $\omega_B\tau$ increases as τ_{Ohm} increases. Combining the magnetization parameter with Equation (28), the relation between the Ohmic timescale τ_{Ohm} and Hall drift timescale τ_{Hall} is obtained. Figure 3 shows that τ_{Hall} decreases with increasing τ_{Ohm} .

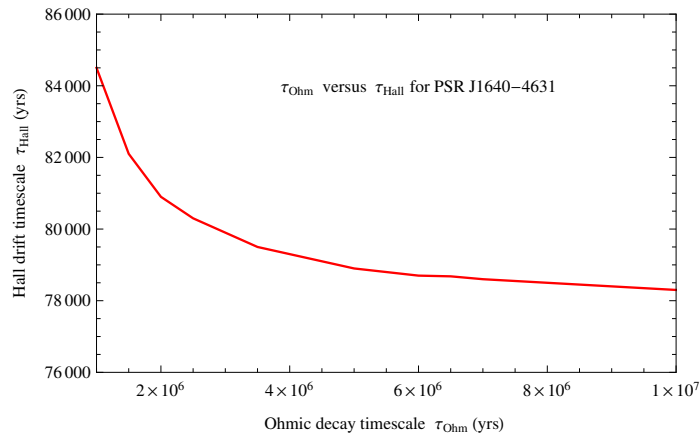


Figure 3. The relation of τ_{Ohm} and τ_{Hall} for PSR J1640-4631.

3.3. Simulating the Dipole Magnetic Field Evolution and Rotation Evolution of PSR J1640-4631

When $t = t_{age} = 3130$ yrs, combining the EoS and arrival time parameters, we obtain the present value of surface dipole magnetic field, $B_p(t_{age}) = (3c^3 I \dot{P} P / 2\pi^2 R^6)^{1/2} \approx 2.305 \times 10^{13}$ G for PSR J1640-4631. Letting the Ohmic dissipation timescale vary between 1.0×10^6 yrs and 3.0×10^7 yrs. Inserting $P(t_{age}) = 0.2064$ ms and $B_p(t_{age}) = 2.305 \times 10^{13}$ G into the expressions of $B_p(t)$ and $P(t)$, we obtain the values of initial dipole magnetic field B_0 and initial spin period P_0 . According to Equation (7), the Ohmic timescale is constrained as $\tau_{Ohm} \in (1.0 \times 10^6 - 9.4 \times 10^6)$ yrs. It is found that, when the Ohmic timescale is arbitrarily available in the range of $(1.0 \times 10^6 - 3.0 \times 10^7)$ yrs, the initial magnetic field B_0 ranges from 2.3752×10^{13} G to 2.3810×10^{13} G, in other words, B_0 is almost constant, and the initial period is distributed in a very narrow range, $P_0 \sim (37.8 - 40.6)$ ms. Then we obtain a mean dipole magnetic field decay rate of the pulsar $\Delta B_p / \Delta t = [B_p(t_{age}) - B_0] / \Delta t \approx -(2.3 - 2.4) \times 10^8$ G yr⁻¹. Some of simulation results are listed in Table 6.

Table 6. Partial fitted values of Ohmic dissipation timescale, Hall drift timescale, magnetization parameter, initial dipole magnetic field, and initial rotational period of PSR J 1640-4631.

τ_{Ohm} (yrs)	τ_{Hall} (yrs)	$\omega_B \tau$	B_0 (G)	$\frac{\omega_B \tau}{(B_0/(10^{13} \text{ G}))}$	P_0 (ms)
1.0e6	8.45e4	11.83	2.3752e13	4.96	40.6
3.0e6	7.99e4	37.57	2.3758e13	15.8	40.4
5.0e6	7.89e4	63.31	2.3768e13	26.5	39.9
6.0e6	7.88e4	76.16	2.3769e13	31.9	39.7
7.0e6	7.86e4	89.05	2.3772e13	37.3	39.4
8.0e6	7.85e4	101.9	2.3774e13	42.7	39.2
9.0e6	7.84e4	114.8	2.3778e13	48.1	38.9
1.0e7	7.83e4	127.6	2.3782e13	53.5	38.4
2.0e7	7.80e4	256.3	2.3802e13	107.6	38.3
3.0e7	7.78e4	385.2	2.3810e13	161.2	37.8

Substituting Equations (19) and (23) simultaneously into Equation (28), we obtain the braking index expression

$$n = 3 + \frac{3Ic^3(\omega_B \tau)^2 Z}{\pi^2 R^6 B_0^2 \tau_{Ohm}} \cdot \frac{a(a - e^{-Zt/\tau_{Ohm}})}{e^{-2Zt/\tau_{Ohm}}} \left[P_0^2 + \frac{4\pi^2 R^6 B_0^2 \tau_{Ohm}}{3Ic^3(\omega_B \tau)^2 Z} [\ln(a - 1) + \frac{a}{a - 1} - \frac{a}{a - e^{-Zt/\tau_{Ohm}}} - \ln(a - e^{-Zt/\tau_{Ohm}})] \right]. \tag{29}$$

From Equation (29), we obtain the relation of the braking index n and time t for PSR J1640-4631, as shown in Figure 4.

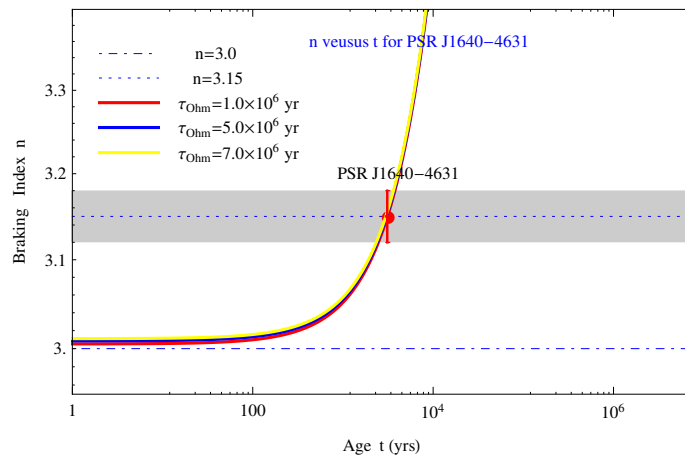


Figure 4. Braking index as a function of t for PSR J1640-4631. Here, the measured value of n is shown with the red dot.

In Figure 4, the blue dot-dashed line stands for the prediction of the MDR model, the horizontal blue dotted line and the surrounding shaded region denote, respectively, the measured braking index of $n = 3.15$ and its possible range given by the uncertainty 0.03 of the star. The solid red line represents the change trend expected by the dipole magnetic field decay model in the case of $\tau_{Ohm} = 1.0 \times 10^6$ yrs, $P_0 = 40.6$ ms and $B_0 = 2.3752 \times 10^{13}$ G, while the solid blue line represents the change trend expected by the dipole magnetic field decay model in the case of $\tau_{Ohm} = 5.0 \times 10^6$ yrs, $P_0 = 39.9$ ms and $B_0 = 2.3768 \times 10^{13}$ G, the solid yellow line represents the change trend expected by the dipole magnetic field decay model in the case of $\tau_{Ohm} = 7.0 \times 10^6$ yrs, $P_0 = 39.4$ ms and $B_0 = 2.3772 \times 10^{13}$ G. As can be seen from Figure 4, the braking index n increases with the increase of t , due to the decay of the dipole magnetic field.

We are more concerned with the dipole magnetic field evolution of PSR J1640-4631. Here we select arbitrarily four different magnetization parameters (1) $\omega_B\tau = 5B_0/(10^{13}\text{ G})$, corresponding to $\tau_{Ohm} = 1.01 \times 10^6\text{ yrs}$, $\tau_{Hall} = 8.44 \times 10^4\text{ yrs}$ and $B_0/(10^{13}\text{ G}) = 2.383$; (2) $\omega_B\tau = 20B_0/(10^{13}\text{ G})$, corresponding to $\tau_{Ohm} = 4.1 \times 10^6\text{ yrs}$, $\tau_{Hall} = 7.94 \times 10^4\text{ yrs}$ and $B_0/(10^{13}\text{ G}) = 2.384$; (3) $\omega_B\tau = 30B_0/(10^{13}\text{ G})$ corresponding to $\tau_{Ohm} = 5.6 \times 10^6\text{ yrs}$, $\tau_{Hall} = 7.88 \times 10^4\text{ yrs}$ and $B_0/(10^{13}\text{ G}) = 2.385$; (4) $\omega_B\tau = 45B_0/(10^{13}\text{ G})$ corresponding to $\tau_{Ohm} = 8.41 \times 10^6\text{ yrs}$, $\tau_{Hall} = 7.84 \times 10^4\text{ yrs}$ and $B_0/(10^{13}\text{ G}) = 2.385$; From Equation (13), we plot the diagrams of B_p versus t for the pulsar in Figure 5.

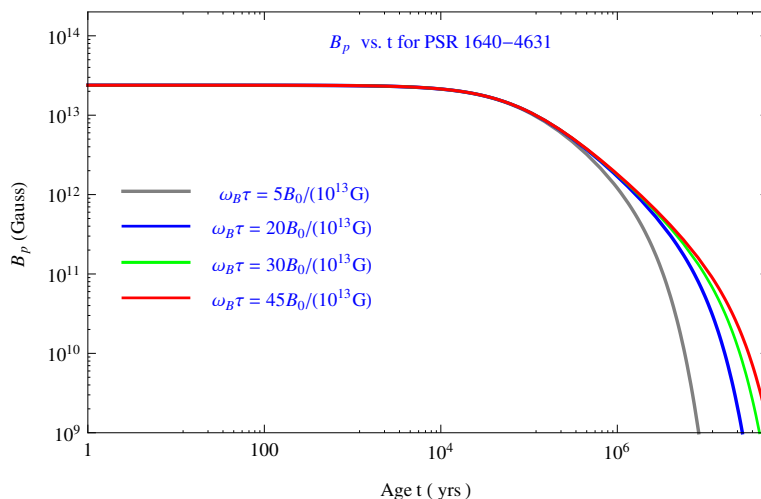


Figure 5. The dipolar magnetic field B_p as a function of t for PSR J1640-4631 with $n > 3$.

From Equation (13), we plot the diagrams of B_p versus t for the pulsar in Figure 5. As can be seen from Figure 5, B_p decreases with the increase in time t . The decay rate of the dipole magnetic field is an important parameter. According to Equation (14), we make a plot of dB_p/dt and time t , as shown in Figure 6.

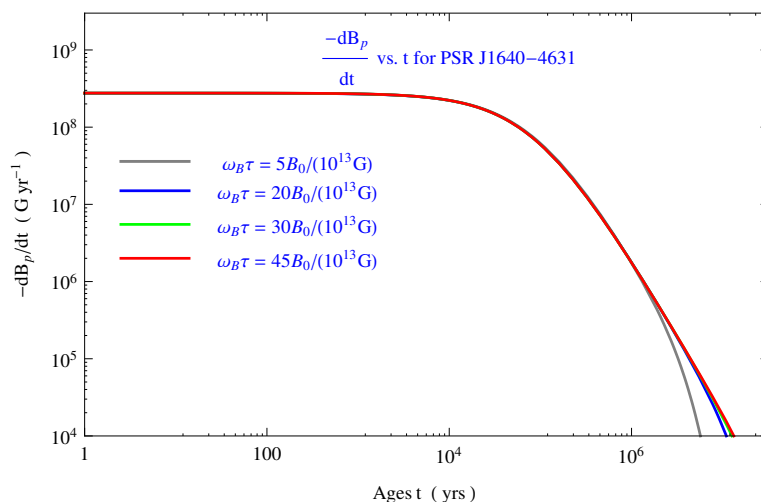


Figure 6. The dipolar magnetic field decay rate dB_p/dt as a function of t for PSR J1640-4631 with $n > 3$.

Figure 6 shows that dB_p/dt decreases with the increase in t . With the combination of Ohmic dissipation and Hall drift, the dipole magnetic energy decay rate, L_p , is then estimated as

$$\begin{aligned}
 L_p &= \frac{-1}{4\pi} \int_V B_p \frac{dB_p}{dt} dV \\
 &= \frac{1}{4\pi} \int_V \left(\frac{B_p^2}{\tau_{Ohm}} + \frac{B_p^3}{\tau_{Hall} B_0} \right) dV \\
 &= \int_V Z B_0^2 \left[\frac{e^{-2Zt/\tau_{Ohm}}}{[(1 + \omega_B \tau(1 - e^{-Zt/\tau_{Ohm}}))]^2} + \frac{e^{-3Zt/\tau_{Ohm}}}{\tau_{Hall}} [(1 + \omega_B \tau(1 - e^{-Zt/\tau_{Ohm}}))] \right]^3 dV, \quad (30)
 \end{aligned}$$

where $dV = 4\pi r^2 dr$, the thickness of the NS inner crust is $R_c \approx 0.7$ km, so the ratio of distance $r/R \sim (0.92-1.0)$ with r the distance from the layer to the star's center. We numerically simulate the relation of the dipole magnetic field energy decay rate L_p versus t , as shown in Figure 7.

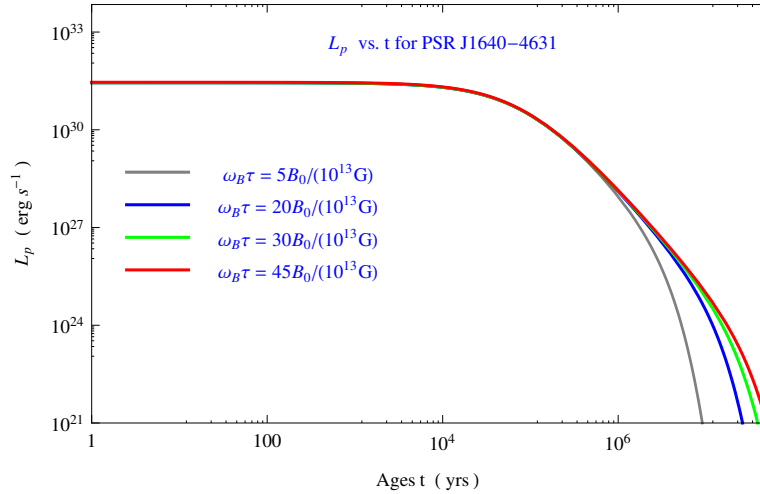


Figure 7. The dipolar magnetic field decay rate L_p as a function of t for PSR J1640-4631 with $n > 3$.

It is obvious that L_p decreases with the increase in t . The differences among three fitted curves are very small, and each curve changes from smoother to steeper, as shown in Figures 5–7. In addition, we calculate the present values of dB_p/dt and L_p : (1) when $\omega_B \tau = 5B_0/(10^{13} \text{ G})$, $dB_p/dt = -2.84 \times 10^8 \text{ G yr}^{-1}$, and $L_p/dt = 2.67 \times 10^{31} \text{ erg s}^{-1}$; (2) when $\omega_B \tau = 20B_0/(10^{13} \text{ G})$, $dB_p/dt = -2.86 \times 10^8 \text{ G yr}^{-1}$, and $L_p/dt = 2.71 \times 10^{31} \text{ erg s}^{-1}$; (3) when $\omega_B \tau = 30B_0/(10^{13} \text{ G})$, $dB_p/dt = -2.88 \times 10^8 \text{ G yr}^{-1}$, and $L_p/dt = 2.78 \times 10^{31} \text{ erg s}^{-1}$; (4) when $\omega_B \tau = 45B_0/(10^{13} \text{ G})$, $dB_p/dt = -2.91 \times 10^8 \text{ G yr}^{-1}$, and $L_p/dt = 2.80 \times 10^{31} \text{ erg s}^{-1}$. It is clear that the dipole magnetic field change rate and magnetic field energy release rate are almost constant (the relative increase rates of $\Delta \dot{B}_p / \dot{B}_p$ and $\Delta L_p / L_p$ are less than 5%).

4. Summary and Comparisons

In this work, we first introduce two different fiducial dipole magnetic fields: $B = 1.0 \times 10^{13} \text{ G}$ and assume that the internal temperature of young highly magnetized NSs cools from $T = 10^9 \text{ K}$ to $1.0 \times 10^8 \text{ K}$ in the first few million years, then calculate the conductivity and magnetization parameter in the NS inner crust and give a general expression of magnetization parameter, magnetic field decay timescales, and magnetic field strength.

As the promotion and application of Equation (7), we assume that the high-braking-index pulsar PSR J1640-4631 is experiencing a dipole magnetic field decay, but the dipole braking still dominates, then establish a theoretical model, and give a constrained Ohmic decay timescale $\tau_{Ohm} \sim (1.0 \times 10^6 - 9.4 \times 10^6) \text{ yrs}$. At last, we numerically simulate the dipole magnetic field

evolution and spin-down evolution of PSR J1640-4631, and compare the fitting results with the observations of the star. Interestingly, in Reference [9], the authors also gave a very practical expression $\tau_{Ohm}/\tau_{Hall} = \omega_B \tau = (1-10)B_0/(10^{13} \text{ G})$. However, Reference [9] ignored the relevant calculations when temperature drops to $T = 10^7 \text{ K}$, and adopted a relatively low impurity concentration range $Q \sim (10^{-4}-10^{-2})$. They also did not consider the effect of magnetic field on Q . Thus, the general expression of magnetization parameter given by this paper may be more close to the actual situation of NSs, compared with that given by Reference [9].

Very recently, in Reference [13], the authors introduced an effective dipole magnetic field decay time scale and adopted the neutron star mass $M \sim (1.0-2.2)M_\odot$ (corresponding to the moment of inertia $I \sim (0.8-2.1) \times 10^{45} \text{ g cm}^2$) in the EoS, and calculated the initial dipole magnetic field range $B_0 \sim (1.84-4.20) \times 10^{13} \text{ G}$ for PSR J1640-4631, the initial rotation period range $P_0 \sim (17-44) \text{ ms}$, and the magnetic field decay rate range $dB_p/dt = -(1.16-3.85) \times 10^8 \text{ G yr}^{-1}$. In order to account for the high braking index of PSR J1640-4631 with a combination of the magneto dipole radiation and dipole magnetic field decay models, Reference [13] introduced a mean rotation energy conversion coefficient ζ , and adopted the APR3 model, which provides a constraint on the maximum NS mass $M_{max} \leq 2.2M_\odot$. By introducing an effective dipole magnetic field decay timescale τ_D , They selected the NS mass $M \sim (1-2.2) M_\odot$, corresponding to $I \sim (0.8-2.09) \times 10^{45} \text{ g cm}^2$, then calculated the star's initial dipole field, $B_0 \sim (1.84-4.20) \times 10^{13} \text{ G}$, the initial spin period $P_0 \sim 17-44 \text{ ms}$, and the magnetic field decay rate $dB_p/dt = -(1.16-3.85) \times 10^8 \text{ G yr}^{-1}$. However, the authors only adopted a simple exponential magnetic field evolution model, and introduced an effective dipole magnetic field decay timescale τ_D , which replaces the special calculations of Ohmic decay timescale and Hall drift timescale, and did not use magnetization parameter to effectively limit the two timescales. Although the calculations in Reference [13] are basically consistent with our results, our results may be more reliable than those in Reference [13]. This study is expected to apply to more young pulsars and will be tested in the future observations.

Author Contributions: H.W. is responsible for organizing, writing and modifying article; Z.-F.G. is responsible for arranging article layout structure, choosing references and writing cover letter; H.-Y.J. is responsible for theoretical analysis, and data processing; N.W. is responsible for making plots and tables and improving language, and X.-D.L. is responsible for theoretical analysis and publication fee. All authors have read and agreed to the published version of the manuscript.

Funding: This work was supported by the National Key Research and Development Program of China (2018YFA04040602, 2018YFA0404202, and 2016YFA0400803), the Natural Science Foundation of China under grant No.11673056, 11773015, 11173042 and 11947404, Xinjiang Natural Science Foundation No.2018D01A24 and Project U1838201 supported by NSFC and CAS.

Acknowledgments: We are grateful the referees for helpful comments.

Conflicts of Interest: The authors declare that there are no conflict of interest.

Appendix A

Table A1. Table 1 Partial values of electrical conductivity and magnetization parameter for two different temperatures T and two different impurity parameters Q in the inner crust of NSs for the nuclear mass models HFB-22, HFB-24 and HFB-26. The unit of magnetization parameter $\omega_B\tau$ is the normalized magnetic field B_{14} when the dipolar magnetic field strength $B = 1.0 \times 10^{14}$ G. Here the crust is assumed to be isothermal.

		5e8 K					1.0e9 K				
		Q = 0.01		Q = 1			Q = 0.01		Q = 1		
\bar{n}_b (fm ⁻³)	ρ (g cm ⁻³)	Y_e	n_e (cm ⁻³)	σ (s ⁻¹)	$\omega_B\tau$						
HFB-22											
2.700e-04	4.513e11	2.955e-01	7.979e34	6.54e22	5.73	6.53e22	5.69	3.54e22	3.08	3.52e22	3.07
5.253e-04	8.790e11	1.839e-01	9.658e34	7.68e22	5.53	7.62e22	5.48	4.07e22	2.93	4.05e22	2.92
8.778e-04	1.470e12	1.294e-01	1.136e35	8.83e22	5.41	8.77e22	5.37	4.62e22	2.83	4.60e22	2.81
1.593e-03	2.670e12	8.832e-02	1.407e35	1.09e23	5.35	1.07e23	5.24	5.53e22	2.73	5.49e22	2.71
2.094e-03	3.510e12	7.511e-02	1.573e35	1.21e23	5.33	1.20e23	5.26	6.08e22	2.69	6.05e22	2.68
2.707e-03	4.540e12	6.510e-02	1.762e35	1.35e23	5.29	1.34e23	5.25	6.74e22	2.66	6.70e22	2.65
3.726e-03	6.250e12	5.526e-02	2.059e35	1.59e23	5.34	1.57e23	5.27	7.81e22	2.64	7.76e22	2.62
4.994e-03	8.380e12	4.826e-02	2.410e35	1.88e23	5.42	1.85e23	5.33	9.11e22	2.62	9.05e22	2.60
8.931e-03	1.500e13	3.841e-02	3.431e35	2.86e23	5.79	2.81e23	5.69	1.33e23	2.69	1.32e23	2.67
1.535e-02	2.580e13	3.221e-02	4.944e35	4.75e23	6.67	4.63e23	6.50	2.11e23	2.96	2.08e23	2.92
2.781e-02	4.680e13	2.696e-02	7.498e35	9.85e23	9.12	9.41e23	8.72	4.10e23	3.80	4.02e23	3.72
3.400e-02	5.725e13	2.562e-02	8.709e35	1.36e24	10.84	1.28e24	10.21	5.51e23	4.39	5.38e23	4.29
HFB-24											
2.570e-04	4.296e11	3.028e-01	7.783e34	6.46e22	5.77	6.41e22	5.72	3.48e22	3.11	3.46e22	3.09
2.788e-04	4.660e11	2.859e-01	7.970e34	6.58e22	5.74	6.53e22	5.69	3.54e22	3.09	3.52e22	3.07
5.253e-04	8.790e11	1.847e-01	9.703e34	7.72e22	5.53	7.65e22	5.48	4.08e22	2.93	4.07e22	2.91
8.778e-04	1.470e12	1.325e-01	1.163e35	9.02e22	5.39	8.95e22	5.34	4.70e22	2.82	4.67e22	2.79
1.194e-03	2.000e12	1.100e-01	1.314e35	1.02e23	5.35	9.98e22	5.28	5.19e22	2.75	5.16e22	2.72
1.593e-03	2.670e12	9.352e-02	1.490e35	1.14e23	5.28	1.13e23	5.23	5.77e22	2.69	5.74e22	2.68
2.707e-03	4.540e12	7.186e-02	1.945e35	1.49e23	5.29	1.47e23	5.22	7.34e22	2.63	7.30e22	2.61
3.724e-03	6.250e12	6.288e-02	2.342e35	1.80e23	5.34	1.78e23	5.28	8.77e22	2.60	8.71e22	2.59
4.991e-03	8.380e12	5.661e-02	2.825e35	2.23e23	5.48	2.20e23	5.41	1.06e23	2.61	1.05e23	2.58
8.926e-03	1.500e13	4.809e-02	4.293e35	3.77e23	6.10	3.69e23	5.97	1.71e23	2.77	1.69e23	2.73
1.534e-02	2.580e13	4.289e-02	6.578e35	7.07e23	7.46	6.83e23	7.21	3.03e23	3.20	2.98e23	3.15
2.778e-02	4.680e13	3.795e-02	1.054e36	1.66e24	10.94	1.55e24	10.21	6.64e23	4.37	6.46e23	4.26
3.000e-02	5.055e13	3.729e-02	1.119e36	1.87e24	11.61	1.74e24	10.80	7.44e23	4.62	7.23e23	4.49
5.000e-02	8.437e13	3.328e-02	1.664e36	4.93e24	20.57	4.27e24	17.82	1.83e24	7.64	1.73e24	7.22
5.634e-02 *	9.510e13 *	3.279e-02	1.847e36	6.65e24	25.00	5.57e24	20.94	2.41e24	9.06	2.25e24	8.46
HFB-26											
2.620e-04	4.379e11	2.996e-01	7.850e34	6.49e22	5.74	6.44e22	5.70	3.48e22	3.09	3.48e22	3.08
2.788e-04	4.660e11	2.866e-01	7.988e34	6.58e22	5.72	6.53e22	5.68	3.54e22	3.08	3.52e22	3.06
5.252e-04	8.790e11	1.833e-01	9.629e34	7.66e22	5.53	7.59e22	5.48	4.04e22	2.93	4.04e22	2.92
8.777e-04	1.470e12	1.298e-01	1.139e35	8.84e22	5.39	8.77e22	5.35	4.61e22	2.81	4.60e22	2.80
1.194e-03	2.000e12	1.066e-01	1.273e35	9.78e22	5.33	9.68e22	5.29	5.06e22	2.76	5.02e22	2.74
1.593e-03	2.670e12	8.955e-02	1.427e35	1.10e23	5.31	1.08e23	5.22	5.56e22	2.71	5.52e22	2.69
2.707e-03	4.540e12	6.698e-02	1.813e35	1.38e23	5.26	1.37e23	5.22	6.87e22	2.64	6.83e22	2.62
3.726e-03	6.250e12	5.756e-02	2.144e35	1.64e23	5.31	1.61e23	5.21	8.04e22	2.61	7.98e22	2.58
4.993e-03	8.380e12	5.098e-02	2.546e35	1.97e23	5.37	1.95e23	5.32	9.51e22	2.59	9.44e22	2.57
8.929e-03	1.500e13	4.224e-02	3.772e35	3.16e23	5.82	3.10e23	5.71	1.45e23	2.67	1.44e23	2.65
1.534e-02	2.580e13	3.758e-02	5.765e35	5.70e23	6.87	5.53e23	6.66	2.47e23	2.98	2.44e23	2.94
2.778e-02	4.680e13	3.456e-02	9.601e35	1.36e24	9.84	1.28e24	9.26	5.41e23	3.91	5.29e23	3.83
3.000e-02	5.054e13	3.425e-02	1.028e36	1.55e24	10.47	1.45e24	9.80	6.11e23	4.13	5.96e23	4.03
5.000e-02	8.437e13	3.278e-02	1.639e36	4.44e24	18.81	3.89e24	16.48	1.62e24	6.86	1.54e24	6.52
5.634e-02 *	9.510e13 *	3.274e-02	1.845e36	6.08e24	22.88	5.15e24	19.38	2.16e24	8.13	2.03e24	7.64

* The sign denotes that the computed equilibrium proton number Z_{eq} begins to deviate from a standard value of $Z = 40$.

Table A2. Table 1 Partial values of electrical conductivity and magnetization parameter for two different temperatures T and two different impurity parameters Q in the inner crust of NSs for the nuclear mass models HFB-22, HFB-24 and HFB-26. The unit of magnetization parameter $\omega_B \tau$ is the normalized magnetic field B_{14} when the dipolar magnetic field strength $B = 1.0 \times 10^{14}$ G. Here the crust is assumed to be isothermal.

\bar{n}_b (fm ⁻³)	ρ (g cm ⁻³)	Y_e	n_e (cm ⁻³)	1e7 K			1.0e8 K				
				Q = 0.01		Q = 1	Q = 0.01		Q = 1		
				σ (s ⁻¹)	$\omega_B \tau$						
HFB-22											
2.700e-04	4.513e11	2.955e-01	7.979e34	4.78e25	4162.2	7.40e24	647.2	5.66e23	49.3	5.32e23	46.3
5.253e-04	8.790e11	1.839e-01	9.658e34	6.20e25	4461.2	8.14e24	588.5	7.02e23	50.5	6.52e23	46.9
8.778e-04	1.470e12	1.294e-01	1.136e35	7.66e25	4688.2	8.79e24	541.2	8.53e23	52.2	7.86e23	48.0
1.593e-03	2.670e12	8.832e-02	1.407e35	1.03e26	5052.5	9.70e24	480.2	1.12e24	54.9	1.02e24	49.9
2.094e-03	3.510e12	7.511e-02	1.573e35	1.19e26	5222.9	1.03e25	452.3	1.29e24	56.7	1.16e24	51.0
2.707e-03	4.540e12	6.510e-02	1.762e35	1.38e26	5441.2	1.07e25	421.7	1.50e24	58.9	1.33e24	52.2
3.726e-03	6.250e12	5.526e-02	2.059e35	1.72e26	5810.2	1.15e25	387.9	1.83e24	61.7	1.59e24	53.7
4.994e-03	8.380e12	4.826e-02	2.410e35	2.16e26	6224.1	1.23e25	354.4	2.28e24	65.7	1.94e24	55.9
8.931e-03	1.500e13	3.841e-02	3.431e35	3.74e26	7569.9	1.44e25	291.5	3.89e24	78.7	3.09e24	62.5
1.535e-02	2.580e13	3.221e-02	4.944e35	7.06e26	9916.6	1.70e25	238.7	7.24e24	101.7	5.11e24	71.8
2.781e-02	4.680e13	2.696e-02	7.498e35	1.66e27	15,374	2.08e25	192.6	1.69e25	156.5	9.36e24	86.7
3.400e-02	5.725e13	2.562e-02	8.709e35	2.39e27	19,058	2.25e25	179.4	2.43e25	193.8	1.17e25	93.3
HFB-24											
2.570e-04	4.296e11	3.028e-01	7.783e34	4.70e25	4182.2	7.31324	654.5	5.55e23	49.5	5.22e23	46.6
2.788e-04	4.660e11	2.859e-01	7.970e34	4.83e25	4198.3	7.41e24	645.7	5.69e23	49.6	5.35e23	46.6
5.253e-04	8.790e11	1.847e-01	9.703e34	6.30e25	4498.1	8.16e24	585.8	7.10e23	50.9	6.60e23	47.3
8.778e-04	1.470e12	1.325e-01	1.163e35	7.98e25	4762.4	8.89e24	533.6	8.84e23	52.9	8.11e23	48.6
1.194e-03	2.000e12	1.100e-01	1.314e35	9.38e25	4956.5	9.40e24	499.5	1.05e24	54.6	9.36e23	49.5
1.593e-03	2.670e12	9.352e-02	1.490e35	1.12e26	5178.6	9.95e24	465.2	1.21e24	56.1	1.10e24	50.9
2.707e-03	4.540e12	7.186e-02	1.945e35	1.61e26	5719.2	1.13e25	402.2	1.72e24	61.2	1.51e24	53.7
3.724e-03	6.250e12	6.288e-02	2.342e35	2.10e26	6197.2	1.23e25	361.8	2.21e24	65.2	1.89e24	55.7
4.991e-03	8.380e12	5.661e-02	2.825e35	2.77e26	6784.7	1.32e25	324.5	2.88e24	70.8	2.39e24	58.8
8.926e-03	1.500e13	4.809e-02	4.293e35	5.32e26	8621.9	1.59e25	257.2	5.49e24	88.8	4.11e24	66.5
1.534e-02	2.580e13	4.289e-02	6.578e35	1.13e27	11,929	1.92e25	202.7	1.15e25	121.4	7.25e24	76.5
2.778e-02	4.680e13	3.795e-02	1.054e36	2.96e27	19,502	2.42e25	159.4	3.00e25	197.7	1.35e25	88.9
3.000e-02	5.055e13	3.729e-02	1.119e36	3.38e27	20,976	2.50e25	155.1	3.44e25	213.5	1.45e25	90.0
5.000e-02	8.437e13	3.328e-02	1.664e36	9.59e27	40,022	3.19e25	133.1	9.85e25	411.1	2.41e25	101.0
5.634e-02 *	9.510e13 *	3.279e-02	1.847e36	1.32e28	49,630	3.43e25	129.0	1.36e26	511.3	2.74e25	103.0
HFB-26											
2.620e-04	4.379e11	2.996e-01	7.850e34	4.72e25	4162.2	7.35e24	649.6	5.57e23	49.2	5.24e23	46.4
2.788e-04	4.660e11	2.866e-01	7.988e34	4.82e25	4175.3	7.41e24	646.9	5.68e23	49.3	5.34e23	46.4
5.252e-04	8.790e11	1.833e-01	9.629e34	6.24e25	4488.8	8.13e24	587.2	7.03e23	50.7	6.54e23	47.2
8.777e-04	1.470e12	1.298e-01	1.139e35	7.75e25	4721.3	8.79e24	537.5	8.60e23	52.5	7.91e23	48.3
1.194e-03	2.000e12	1.066e-01	1.273e35	8.99e25	4895.8	9.26e24	506.1	9.87e23	53.8	9.01e23	49.1
1.593e-03	2.670e12	8.955e-02	1.427e35	1.06e26	5112.0	9.72e24	475.5	1.15e24	55.6	1.04e24	50.2
2.707e-03	4.540e12	6.698e-02	1.813e35	1.46e26	5556.1	1.10e25	419.6	1.56e24	59.5	1.38e24	52.6
3.726e-03	6.250e12	5.756e-02	2.144e35	1.84e26	5959.8	1.17e25	379.0	1.95e24	63.2	1.69e24	54.4
4.993e-03	8.380e12	5.098e-02	2.546e35	2.36e26	6437.1	1.26e25	343.7	2.48e24	67.6	2.09e24	57.0
8.929e-03	1.500e13	4.224e-02	3.772e35	4.33e26	7971.8	1.50e25	276.2	4.47e24	82.3	3.47e24	63.9
1.534e-02	2.580e13	3.758e-02	5.765e35	8.95e26	10,781	1.80e25	216.8	9.13e24	110.0	6.10e24	73.5
2.778e-02	4.680e13	3.456e-02	9.601e35	2.44e27	17,649	2.29e25	165.6	2.48e25	179.4	1.20e25	86.8
3.000e-02	5.054e13	3.425e-02	1.028e36	2.83e27	19,117	2.37e25	160.1	2.87e25	193.9	1.31e25	88.5
5.000e-02	8.437e13	3.278e-02	1.639e36	8.88e27	37,624	3.09e25	130.9	9.10e25	385.6	2.31e25	97.9
5.634e-02 *	9.510e13 *	3.274e-02	1.845e36	1.23e28	46,296	3.34e25	125.7	1.27e26	478.0	2.65e25	99.7

* The sign denotes that the computed equilibrium proton number Z_{eq} begins to deviate from a standard value of $Z = 40$.

References

1. Goldreich, P.; Reisenegger, A. Magnetic field decay in isolated neutron stars. *Astrophys. J.* **1992**, *395*, 250–258.
2. Duncan, R.C.; Thompson, C. Formation of very strongly magnetized neutron stars—Implications for gamma-ray bursts. *Astrophys. J.* **1992**, *392*, L9–L13.

3. Thompson, C.; Duncan, R.C. The soft gamma repeaters as very strongly magnetized neutron stars. II. Quiescent neutrino, X-ray, and Alfvén wave emission. *Astrophys. J.* **1996**, *473*, 322–342.
4. Gourgouliatos, K.N.; Cumming, A. Hall attractor in axially symmetric magnetic fields in neutron star crusts. *Phys. Rev. Lett.* **2014**, *112*, 171101.
5. Gao, Z.-F.; Peng, F.-K.; Wang, N. The evolution of magnetic field and spin-down of young pulsars. *Astron. Nachr.* **2019**, *340*, 1023–1029.
6. Gao, Z.-F.; Omar, N.; Shi, X.-C.; Wang, N. The Ohmic decay of dipolar toroidal magnetic fields of magnetars. *Astron. Nachr.* **2019**, *340*, 1030–1034.
7. Liu, J.-J.; Liu, D.-M. Supernova β -decay of nuclide ^{53}Fe , ^{54}Fe , ^{55}Fe , and ^{56}Fe in strongly screening plasma. *Res. Astron. Astrophys.* **2018**, *18*, 8–13.
8. Liu, J.-J.; Liu, D.-M.; Hao, L.-H. Strongly screening β -decay antineutrino energy loss in presupernova. *Chin. Phys. C* **2019**, *43*, 064107
9. Pons, J.A.; Geppert, U. Magnetic field dissipation in neutron star crusts: From magnetars to isolated neutron stars. *Astron. Astrophys.* **2007**, *470*, 303–315.
10. Page, D.; Geppert, U.; Weber, F. The cooling of compact stars. *Spec. Issue Nucl. Astrophys.* **2006**, *777*, 497–530.
11. Page, D.; Lattimer, J.M.; Prakash, M.; Steiner, A.W. Neutrino emission from Cooper pairs and minimal cooling of neutron stars. *Astrophys. J.* **2009**, *707*, 1131–1140.
12. Gao, Z.F.; Li, X.D.; Wang, N.; Yuan, J.P.; Wang, P.; Peng, Q.H.; Du, Y.J. Constraining the braking indices of magnetars. *Mon. Not. R. Astron. Soc.* **2016**, *456*, 55–65.
13. Gao, Z.F.; Wang, N.; Shan, H.; Li, X.D.; Wang, W. The Dipole Magnetic Field and Spin-down Evolutions of the High Braking Index Pulsar PSR J1640–4631. *Astrophys. J.* **2017**, *849*, 19.
14. Liu, J.-J.; Liu, D.-M. Magnetar crust electron capture for ^{55}Co and ^{56}Ni . *Eur. Phys. J. C* **2018**, *78*, 84.
15. Urpin, V.A.; Chanmugam, G.; Sang, Y. Long-term evolution of crustal neutron star magnetic fields. *Astrophys. J.* **1994**, *433*, 780–785.
16. Liu, J.-J.; Gu, W.-M. A New Insight into Neutrino Energy Loss by Electron Capture of Iron Group Nuclei in Magnetar Surfaces. *Astrophys. J. Suppl. Ser.* **2016**, *224*, 29–43. [[CrossRef](#)]
17. Muslimov, A.; Page, D. Magnetic and Spin History of Very Young Pulsars. *Astrophys. J.* **1996**, *458*, 347–354. [[CrossRef](#)]
18. Mitra, D.; Konar, S.; Bhattacharya, D. Evolution of the multipolar magnetic field in isolated neutron stars. *Mon. Not. R. Astron. Soc.* **1999**, *307*, 459–462. [[CrossRef](#)]
19. Geppert, U.; Urpin, V. Accretion-driven magnetic field decay in neutron stars. *Mon. Not. R. Astron. Soc.* **1994**, *271*, 490–498. [[CrossRef](#)]
20. Konar, S.; Bhattacharya, D. Magnetic field evolution of accreting neutron stars. *Mon. Not. R. Astron. Soc.* **1997**, *284*, 311–317. [[CrossRef](#)]
21. Geppert, U.; Page, D.; Zannias, T. Magnetic field decay in neutron stars: Analysis of general relativistic effects. *Phys. Rev. D* **2000**, *61*, 123004. [[CrossRef](#)]
22. Aguilera, D.N.; Pons, J.A.; Miralles, J.A. 2D Cooling of magnetized neutron stars. *Astron. Astrophys.* **2008**, *486*, 255–271. [[CrossRef](#)]
23. Beloborodov, A.M.; Li, X. Magnetar Heating. *Astrophys. J.* **2016**, *833*, 261–281. [[CrossRef](#)]
24. Pons, J.A.; Viganò, D. Magnetic, thermal and rotational evolution of isolated neutron stars. *Living Rev. Comput. Astrophys.* **2019**, *5*, 3. [[CrossRef](#)]
25. Wang, H.; Gao, Z.; Wang, N.; Jia, H.; Li, X.; Zhi, Q. Investigations of the Ohmic Decay and the Soft X-Ray Emission of the High-braking-index Pulsar PSR J1640–4631. *Publ. Astron. Soc. Pac.* **2019**, *131*, 054201. [[CrossRef](#)]
26. Chen, J.-L.; Wang, H.; Jia, H.-Y.; Ma, Z.-W.; Li, Y.-H.; Tan, J. Conductivity of neutron star crust under superhigh magnetic fields and Ohmic decay of toroidal magnetic field of magnetar. *Acta Phys. Sin.* **2019**, *68*, 180401.
27. Viganò, D.; Rea, N.; Pons, J.A.; Perna, R.; Aguilera, D.N.; Miralles, J.A. Unifying the observational diversity of isolated neutron stars via magneto-thermal evolution models. *Mon. Not. R. Astron. Soc.* **2013**, *434*, 123–141. [[CrossRef](#)]
28. Ho, W.C.G. Evolution of a buried magnetic field in the central compact object neutron stars. *Mon. Not. R. Astron. Soc.* **2011**, *414*, 2567–2575. [[CrossRef](#)]

29. Pons, J.A.; Miralles, J.A.; Geppert, U. Magneto-thermal evolution of neutron stars. *Astron. Astrophys.* **2009**, *496*, 207–216. [[CrossRef](#)]
30. Yakovlev, D.G.; Shalybkov, D.A. Electrical conductivity of neutron star cores in the presence of a magnetic field. *Astrophys. Space Sci.* **1991**, *176*, 191–215. [[CrossRef](#)]
31. Flowers, E.; Itoh, N. Transport properties of dense matter. III-Analytic formulae for thermal conductivity. *Astrophys. J.* **1981**, *250*, 750–752. [[CrossRef](#)]
32. Goriely, S.; Chamel, N.; Pearson, J.M. Further explorations of Skyrme-Hartree-Fock-Bogoliubov mass formulas. XII. Stiffness and stability of neutron-star matter. *Phys. Rev. C* **2010**, *82*, 035804. [[CrossRef](#)]
33. Pearson, J.M.; Chamel, N.; Potekhin, A.Y.; Fantina, A.F.; Ducoin, C.; Dutta, A.K.; Goriely, S. Unified equations of state for cold non-accreting neutron stars with Brussels—Montreal functionals—I. Role of symmetry energy. *MNRAS* **2018**, *481*, 2994–3026. [[CrossRef](#)]
34. Wang, M.; Audi, G.; Kondev, F.G.; Huang, W.J.; Naimi, S.; Xu, X. The AME2016 atomic mass evaluation (II). Tables, graphs and references. *Chin. Phys. C* **2017**, *41*, 030003. [[CrossRef](#)]
35. Antoniadis, J.; Freire, P.C.; Wex, N.; Tauris, T.M.; Lynch, R.S.; van Kerkwijk, M.H.; Hessels, J.W. A massive pulsar in a compact relativistic binary. *Science* **2013**, *340*, 1233232. [[CrossRef](#)]
36. Li, Z.-H.; Schulze, H.-J. Neutron star structure with modern nucleonic three-body forces. *Phys. Rev. C* **2008**, *78*, 028801. [[CrossRef](#)]
37. Akmal, A.; Pandharipande, V.R.; Ravenhall, D.G. Equation of state of nucleon matter and neutron star structure. *Phys. Rev. C* **1998**, *58*, 1804–1828. [[CrossRef](#)]
38. Potekhin, A.Y.; Pons, J.A.; Page, D. Neutron Stars—Cooling and Transport. *Space Sci. Rev.* **2015**, *191*, 239–291. [[CrossRef](#)]
39. Alpar, M.A.; Baykal, A. Pulsar braking indices, glitches and energy dissipation in neutron stars. *Mon. Not. R. Astron. Soc.* **2006**, *372*, 489–496. [[CrossRef](#)]
40. Chen, W.C.; Li, X.D. Why the braking indices of young pulsars are less than 3? *Astron. Astrophys.* **2006**, *450*, L1–L4. [[CrossRef](#)]
41. Gotthelf, E.V.; Tomsick, J.A.; Halpern, J.P.; Gelfand, J.D.; Harrison, F.A.; Boggs, S.E.; Stern, D.K. NuSTAR discovery of a young, energetic pulsar associated with the luminous gamma-ray source HESS J1640-465. *Astrophys. J.* **2014**, *788*, 155–163. [[CrossRef](#)]
42. Archibald, R.F.; Gotthelf, E.V.; Ferdman, R.D.; Kaspi, V.M.; Guillot, S.; Harrison, F.A.; Omsick, J.A. A high braking index for a pulsar. *Astrophys. J. Lett.* **2016**, *819*, L16–L19. [[CrossRef](#)]
43. Castelletti, G.; Giacani, E.; Dubner, G.; Joshi, B.C.; Rao, A.P.; Terrier, R. First high-resolution radio study of the supernova remnant G338.3-0.0 associated with the gamma-ray source HESS J1640-465. *Astron. Astrophys.* **2011**, *536*, A98. [[CrossRef](#)]
44. Zhao, X.-F. The Composition of Baryon in the Proto Neutron Star PSR J0348+ 0432. *Int. J. Theor. Phys.* **2019**, *58*, 1060–1070. [[CrossRef](#)]
45. Zhao, X.-F. Effect of mesons on the baryons distribution in the massive NS PSR J0348+ 0432. *Astrophys. Space Sci.* **2019**, *364*, 38. [[CrossRef](#)]
46. Zhao, X.-F. The hyperon coupling constants and the surface gravitational redshift of massive neutron stars. *Chin. J. Phys.* **2020**, *63*, 240–247. [[CrossRef](#)]
47. Geng L, Toki, H., Meng, J. Masses, Deformations and Charge Radii—Nuclear Ground-State Properties in the Relativistic Mean Field Model. *Prog. Theor. Phys.* **2005**, *113*, 785–800. [[CrossRef](#)]
48. Kumar, B.; Singh, S.K.; Agrawal, B.K.; Patra, S.K. New parameterization of the effective field theory motivated relativistic mean field model. *Nucl. Phys. A* **2017**, *966*, 197. [[CrossRef](#)]

